Integrated Computational Fluid Dynamics and 1D Process Modelling for Superheater Region in Recovery Boiler

Kunal Kumar

School of Engineering

Thesis submitted in partial fulfillment of the requirements for the degree of Master of Science in Technology.

Espoo 16.05.2019

Supervisor

Prof. Ville Vuorinen

Advisor

Viljami Maakala, D.Sc. (Tech.)

Aalto University
School of Engineering

Aalto University
School of Engineering

Aalto University, P.O. BOX 11000, 00076 AALTO
www.aalto.fi
Abstract of the master's thesis

Author Kunal Kumar

Title Integrated Computational Fluid Dynamics and 1D Process Modelling for Superheater Region in Recovery Boiler

Degree programme Mechanical Engineering

Major Mechanical Engineering **Code of major** ENG25

Supervisor Prof. Ville Vuorinen

Advisor Viljami Maakala, D.Sc. (Tech.)

Date 16.05.2019 **Number of pages** 84 **Language** English

Abstract

Superheaters are the last heat exchangers on the steam side in recovery boilers. Their performance is accountable for proficient recovery boiler operation. The objective of this work is to obtain thorough knowledge about the superheating process and material temperature distribution for superheater platens. The study includes the effects of 3D flue gas flow field in superheater region and generated steam properties in steam cycle. The detailed analysis for flue gas side and steam side is important for improving recovery boilers′ energy efficiency, cost efficiency, safety and contribution for carbon neutral energy production.

In this work, for the first time, a comprehensive 1D-process model (1D-PM) for superheated steam cycle is developed and linked with a full-scale 3D-CFD model of the superheater region flue gas flow. The developed 1D-PM is validated using reference data including mass and energy balance calculations, and measurements.

The results reveal that first; the geometrical structures of headers, connecting pipes and superheater platens affect platen-wise steam distribution. Second, the integrated solution of the 3D flue gas flow field and platen heat flux distribution with the 1D-PM substantially affect both generated superheated steam properties and material temperature distribution. It is also found that the commonly used uniform heat flux distribution approach for superheating process is not accurate because it does not consider the effect of flue gas flow field in superheater region.

This novel integration modelling approach is advantageous for trouble shooting, optimizing the performance of superheaters in recovery boiler and selecting their design margins for the future. It could also be applied for other large scale energy production units including industrial biomass fired boilers.

Keywords Computational fluid dynamics (CFD), 1D-process modelling (1D-PM), integrated CFD/1D-PM simulations, heat transfer, recovery boiler

Acknowledgements

This master thesis project was carried out between May 2018 and May 2019 in the Research and Development Group of the Recovery Boilers Product Group at Andritz Oy, Finland. I would like to express my gratitude to my employer Andritz and manager M.Sc. Jukka Röppänen for providing me this opportunity where I could work on a challenging project as well as improve my technical and interpersonal skills.

I would like to thank my supervisor Professor Ville Vuorinen and my advisor D.Sc. Viljami Maakala for their support and guidance during the work. I especially thank to them for answering my queries and reviewing my work. Moreover, I wish to thank M.Sc. Antti Sirainen and M.Sc. Hu Kexin for their guidance throughout the work. I am also thankful to Lic.Sc. Jari Lappalainen and M.Sc. Ville Hovi from VTT Technical Research Centre of Finland for their support and guidance in Apros 6 and integrated CFD/1D-PM modelling approach that is developed during this work.

I wish to express my gratitude to my colleagues for their generosity. I am grateful to my family and friends, who have been very supportive during my studies. Finally, I dedicate this work to my grandfather Mr. Omkar. S. Yadav.

Helsinki, 16.05.2019

Kunal Kumar

Contents

Symbols and abbreviations

Symbols

Latin

a_λ	Absorption coefficient
c_p	Specific heat
C_s	Roughness constant
d	Inner diameter of tube
$D_{i,m}$	Mass diffusion coefficient
$D_{T,i}$	Thermal diffusion coefficient
E	Radiative emissive power
E	Internal energy
F	Body forces
f	Friction factor
g	Gravitational acceleration
H	Elevation from the ground
h	Enthalpy
h_i	Enthalpy of the flue gas species
I	Radiation intensity
J_i	Species diffusion flux
k	Turbulent kinetic energy
K_s	Roughness height
K	Form loss coefficient
L	Superheater tube length
m	Number of superheater platens
$\dot{m}$	Mass flow rate
n	Refractive index
n	Number of tubes in superheater platen
n_{row}	Number of tube rows in flow direction
p	Pressure
P	Porosity
q	Heat transfer
q''	Heat flux
R	Radius
R_i	Species reaction term
Re	Reynolds number
$\vec{r}$	Position vector
Sc_t	Turbulent Schmidt number
S	Source term
$\vec{s}$	Direction vector
T	Temperature
t	Time
u	Velocity
V	Volume
Y_i	Species mass fraction
X, Y and Z	Coordinates

Greek

β	Convective heat transfer coefficient
γ	Thermal conductivity
γ_{eff}	Effective thermal conductivity
γ_t	Turbulent thermal conductivity
δ	Thickness
ε	Turbulent dissipation rate
ζ	Inertial loss coefficient
η	Relative roughness
μ	Dynamic viscosity
μ_t	Turbulent or eddy viscosity
μ_{eff}	Effective viscosity
ρ	Density
σ	Stefan-Boltzmann constant
σ_s	Scattering coefficient
τ_{eff}	Stress tensor
ϕ	Phase function
ω	Emissivity
Ω'	Solid angle

Subscripts

arc	Arc
b	Black body
$cond$	Conduction
$conv$	Convection
$deposit$	Deposit
$fluid$	Fluid
gas	Flue gas
in	Inlet
$mixture$	Water-steam mixture
out	Outlet
$platen$	Superheater platen
rad	Radiation
ref	Free stream
s	Surface
sur	Surrounding
$solid$	Solid
$total$	Total or sum
$tube$	Tube
w	Wall
$water$	Water
λ	Wavelength

Abbreviations

BFB	Bubbling fluidized bed
BLDS	Black liquor dry solids
CFD	Computational fluid dynamics
HHV	Higher heating value
MHEM	Macro heat exchanger model
NTU	Number of transfer units
RANS	Reynolds-Averaged Navier-Stokes equations
RTE	Radiative transfer equation
UDF	User-defined function
WSGG	Weighted sum of gray gases
1D-PM	1D-process modelling or 1D-process model

Chapter 1

Introduction

1.1 Motivation

Recovery boilers are used to combust black liquor for chemical recovery and producing high pressure superheated steam for power generation. Black liquor is a by-product of kraft pulping process. It comprises of organic dissolved wood residues e.g. lignocellulosic residues, and inorganic cooking chemicals used in pulping process. According to Food and Agriculture Organisation of United Nations (FAO), the global production of chemical wood pulp in 2017 was about 142 million tonnes (see Figure 1.1) [1]. Tran et al. [2] noted that approximately 1.5 kg of black liquor dry solids (BLDS) are produced per 1.0 kg of chemical wood pulp production and 3.5 kg of superheated steam is generated per 1.0 kg of BLDS combustion in recovery boilers. Therefore, 213 million tonnes of BLDS was combusted and 746 million tonnes of superheated steam was generated in 2017. Along with utilization for self-sustainable mill operations, the generated steam is also used for electricity production. For instance, in Finland in 2017, 8.1% of total electricity was generated with black liquor combustion in recovery boilers (Statistics Finland, 2018) [3].

Global production of chemical wood pulp has been forecasted to increase annually by 1%, which is directly related to boost in BLDS production [4]. Hence, black liquor is a vital biomass based renewable energy source from future perspective. Simultaneously, the capacity of recovery boilers has increased since last decades (see Figure 1.1). The current largest capacity of a recovery boiler is 12000 tonnes black liquor dry solids per day (tds/d) and even larger recovery boilers have been planned. Consequently, it is important to develop new computational models for such large boilers to understand their combustion and heat transfer phenomena in detail and also from the perspective of improving their contribution for renewable energy production.

The computational fluid dynamics (CFD) modelling approach has been adopted to analyse the performance of recovery boilers including furnace combustion, heat transfer and deposition since last decades. However, it is very expensive and challenging

to model its water-steam side with CFD due to very large and complex geometries of water-steam circulation sections. On the other hand, 1D-process modelling methods have been utilized for steady state and dynamic simulations of whole power plants. A detailed review of 1D-process modelling is provided by Alobaid et al. [5]. In these 1D simulations, the effects of three-dimensional flow field, temperature and heat flux distribution are usually ignored or simplified. However, the geometries such as pipes, where the established experimental correlations are available, this approach has been shown to be very successful (Alobaid et al. [5], Emara-Shabaik et al. [6], Zima et al. [7] and Bhambare et al. [8]). The integrated CFD/1D-process modelling approach is often adopted to alleviate the above mentioned challenges where a flue gas side 3D-CFD model is coupled with a 1D-process model (1D-PM) of water-steam side.

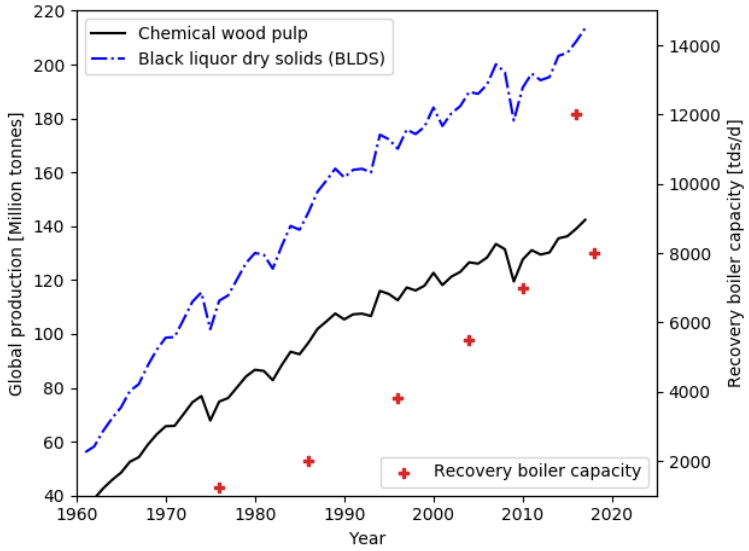

Figure 1.1: Global production of chemical wood pulp and black liquor dry solids (1961-2017) based on FAO data [1, 2], and increment in recovery boiler capacity (1976-2018) [9].

The superheater region in recovery boiler is the main focus of this work. The superheaters are used to produce superheated steam by capturing heat from flue gas. They are the last heat exchangers before the steam turbine. They are made of expensive materials due to the high steam temperature and challenges associated with ash-induced corrosion. Their performance is accountable for efficient and safe recovery boiler power plant operation. Therefore, detailed knowledge of steam properties and material temperature distribution is essential for higher quality superheated steam production, reduction in material issues such as corrosion and improving thermal efficiency of the boiler.

In this work, a full-scale 3D-CFD model of superheater region is coupled with a comprehensive 1D-PM to perform detailed analysis for flue gas side and steam side in superheater region. This integration modelling approach is the novelty of this work.

1.2 Integrated CFD/1D-process modelling

This section describes different CFD modelling approaches for heat transfer sections including superheaters, and results of some integrated or coupled fluid-fluid heat transfer simulations in context of steam boilers.

To begin with, it is a very challenging task to accurately model heat transfer sections of boilers because of their complicated geometries and large dimensions. A widely adopted method is the distributed resistance approach or porous media method that was developed by Patankar et al. [10]. Its prerequisite parameters are volumetric heat sink values, volumetric porosities, surface permeabilities and inertial loss coefficients that are evaluated from design data or measurements.

The porous media method has been substantially utilized either as standalone or coupled with steam cycle to simulate heat transfer sections. Several researchers (Yin et al. [11], Le Bris et al. [12], Díez et al. [13] and Choi et al. [14]) studied the combustion, flow field and pollutant formation e.g. NO_X formation in large scale pulverized coal-fired boilers. The heat transfer sections in these studies were modelled as porous media.

Drosatos et al. [15] simulated the effect of convective heat transfer sections′ geometries on flue gas side and calculated the fluid outlet temperature for these sections using the macro heat exchanger model (MHEM) in a coal fired boiler. The MHEM calculates pressure losses using the porous media method and heat transfer using the number of transfer units (NTU) for tube bundles. The simulated fluid outlet temperature and heat flux to surfaces deviated from boiler operating data by less than 6%. The size and number of computational cells within each macro were accountable for these discrepancies. However, the MHEM does not provide the working fluid temperature distribution along the tube length as the tubes are not modelled separately.

From integrated CFD/1D-PM modelling perspective, various studies for analysing and optimizing the furnace combustion, heat transfer phenomena, steam generation and overall efficiency of steam boilers have been performed since last years. The heat transfer surfaces were often modelled as porous media. Either one-way coupling or two-way coupling has been applied to define the connection between the two calculation models. In the one-way coupling method, only one calculation model transfers the required parameters and does not receive any feedback from the other calculation model. In the two-way coupling method, both calculation models exchange the required parameters. The exchange parameters are usually mass flow rates, pressure and turbulence properties in flow coupling whereas temperature distribution, heat transfer rate and heat flux distribution belong to heat transfer coupling.

Park et al. [16] studied the effect of burner arrangement, coal blending and firing patterns on overall efficiency of an 800 MWe coal fired boiler. The superheaters, economizers and other heat exchangers were modelled as porous media and linked to steady state 1D steam cycle by exchanging heat flux and temperature distribution. The results were validated at full load conditions. It was found that outlet steam

properties e.g. temperature and pressure, and heat absorbed by heat transfer sections deviated by 4% and maximum of 7% respectively. The results also revealed that the proper selection of fouling factors for heat transfer surfaces is essential to improve the numerical accuracy of the model.

Edge et al. [17] developed a 1D-PM and studied steam generation in a 500 MWe natural circulating coal-fired boiler. The 3D heat flux distribution calculated by a CFD model at water walls and heat exchangers′ surfaces was regressed into 1D as a function of boiler height and used for steam side calculations. The regression approach simplified the coupling process and eliminated the dependency of the 1D-PM on computational cells′ positions in the CFD model. The results were compared with an in-house code and reduction of 5% in total heat transfer to 1D steam cycle was found. Moreover, the non-uniformity in 3D heat flux distribution significantly affected the steam generation process because it is responsible for evaporation point location and steam quality.

Schuhbauer et al. [18] linked a dynamic and heterogeneous method based 1D water-steam cycle with a 3D-CFD furnace model of a coal fired boiler and performed coupled simulations using a two-way heat transfer coupling method. The heterogeneous model solves the fluid dynamical equations for water and steam separately. The heat transfer sections were modelled as porous media and their inertial loss coefficients were calculated iteratively until the corresponding pressure losses reached the designed values. The simulation results fitted well with thermodynamic design data. The results revealed that the porous media method did not solve radiation accurately as the tube surfaces were not physically present in the porous media.

Hovi et al. [19] performed transient integrated CFD/1D-PM simulations to investigate the effects of rapid load change (1.9 MW/min) situations on flue gas temperature, temperature distribution on heat transfer sections and pollutant formation in a bubbling fluidized bed (BFB) boiler. The two-way coupling method including flow and heat transfer couplings was utilized. The CFD side results were compared with previous simulations. The results showed that the coarse discretization of the 1D-PM makes the CFD side wall temperature distribution non-uniform and affects the overall simulation accuracy.

Yang et al. [20] performed coupled simulations to analyse the temperature distribution on furnace walls and the heating process of supercritical CO2 (S-CO2) in a conceptual higher efficiency ($\geq 50\%$) coal fired boiler. The results revealed good agreement with literature and thermodynamic design data.

Chen et al. [21] analysed coupled heat transfer phenomena between combustion and platen superheaters in a coal fired boiler. The platen superheaters were modelled as flat plates, and other superheaters and reheaters were modelled using porous media method. A semi-detailed and steady state 1D-PM for platen superheaters was developed where one large tube represented four thin and seamless tubes. Deposition was considered and two-way heat transfer coupling method was utilized. The results fitted well with the measurement data. The calculated steam temperature was

underestimated by 2%. It was also reported that the steam outlet temperature is largely affected by the deposit thickness, its thermal conductivity and temperature.

In addition to steam boilers, the porous media method has also been used in nuclear reactor simulations. Hovi et al. [22] studied coupled heat transfer between the primary tubes (hot fluid) and secondary circuit (cold water) for steam generators in pressurized water reactor. The primary tubes were modelled as porous media and linked with 1D-PM using the surface temperature distribution. The results revealed good agreement with measurement data under steady and transient pressure conditions.

Apart from the porous media method, the 3D slice superheater region model is another simplified approach, which has been used mainly in recovery boiler simulations. In this approach, a 3D thin slice between two superheater platens from the middle of the boiler is considered for simulations. Saviharju et al. [23] analysed the flow field and temperature distribution in the upper furnace for two recovery boilers and compared the results with measurements. Leppänen et al. [24, 25, 26, 27] applied this approach, and studied deposit formation and deposit growth in recovery boilers. The simulation results were also validated with experimental data. Maakala et al. [28] used the slice superheater region model with surrogate-based analysis and optimization to optimize the superheater regions′ geometry and heat transfer. The optimization study revealed 5% increment in heat transfer.

Furthermore, a detailed 3D-CFD model for the superheater region in a recovery boiler was developed by Maakala et al. [29]. All the superheater platens were modelled as flat plates instead of tightly spaced thin tubes to reduce the complexity of simulations. The grid convergence study using grid convergence index (GCI) method was carried out to computationally verify the developed model. The simulation results also fitted well with two sets of measurements. The full superheater region model is advantageous as it provides: a) detailed solution for flow field, radiation and convective heat transfer and b) 3D temperature and heat flux distribution in the superheater region.

1.3 Noted research gaps

The following gaps in the previous research are identified. First, the integrated CFD/1D-PM modelling approaches are state-of-the-art to analyse and optimize the heat transfer sections including superheaters, steam generation and overall performance of coal-fired power plants, BFB boilers and nuclear reactors. However, the effects of the flue gas side on the steam cycle and vice versa have not been well explored in the context of the superheater region in recovery boilers. In fact, as recovery boilers are one of the major contributors ($\geq 25\%$) for industrial biomass based energy production reported by Vakkilainen et al. [30, p. 29], it is highly important to apply such methods in their development process.

Second, most of the standalone CFD and integrated CFD/1D-PM simulations of heat transfer surfaces are based on simplified or semi-detailed methods. The porous media

method is a good approach due to efficient computation time and cost. However, improper prediction of radiation, no detailed analysis for flow field and surface temperature distribution of tube bundles, and requirement of precise calculations for prerequisite parameters are some of its major disadvantages. In the superheater region of a recovery boiler, the evaluation of prerequisite parameters is very challenging due to complex geometries and non-uniform deposition on heat transfer surfaces. In addition, the 3D slice superheater region model does not provide detailed analysis of 3D flow field, temperature distribution and heat transfer. It is only valid when the superheater region has uniform flue gas flow and flow field is insignificantly affected by side walls (Maakala et al. [29]). Similarly, the detailed 3D superheater region model developed by Maakala et al. [29] does not consider the effect of flue gas side on steam cycle and vice versa.

1.4 Objectives of the thesis

The main purpose of this work is to improve the understanding about heat transfer between the hot flue gas and steam cycle by considering the effects of three-dimensional flow field, temperature distribution and circulating steam properties.

The objectives of the thesis are as follows:

1. Develop a comprehensive steam side 1D-PM for the superheater region in a recovery boiler and validate it with reference data.
2. Study the effect of the header and piping arrangement on the platen-wise steam distribution and obtain a baseline temperature distribution for the superheater material.
3. Develop a detailed 3D-CFD model for the superheater region.
4. Perform integrated CFD/1D-PM simulations and
    - Obtain solutions for the flue gas side and steam side including the platen-wise steam distribution and superheater material temperature distribution.
    - Compare the integrated simulation results with the baseline estimation.
    - Discuss the effects of the integrated simulation approach on both the flue gas side and steam side solutions.
5. Discuss the feasibility of the integrated CFD/1D-PM modelling approach and point out its added-value.

Chapter 2

Recovery Boiler Process

In the kraft pulping process, the wood along with white liquor, a mixture of sodium sulphide (Na_2S) and sodium hydroxide (NaOH), is processed for pulp production. In this process, almost half of the wood especially lignin, spent cooking chemicals and water form a liquid stream known as weak black liquor. The weak black liquor is then treated in the evaporation plants to increase its dry solids from 15-20% to 65-85% [31, p. 3]. The concentrated black liquor is burned in a recovery boiler for chemical recovery and steam production for power generation.

Figure 2.1 shows a modern recovery boiler with its important regions and components. The recovery boiler comprises of two sections named as furnace section (1) and heat transfer section (11). The nose arch (7) separates these sections.

2.1 Black liquor combustion

The combustion of black liquor is completed in the furnace section. The liquor guns spray the black liquor as coarse droplets into the furnace. The larger diameter of black liquor droplets (0.5-5 mm) helps to land them on char bed. The smaller diameters are avoided as they can entrain in flue gas flow and contribute for deposition and plugging of the recovery boiler [31, p. 131]. The black liquor combustion completes in three stages, a) drying, b) devolatization (pyrolysis) and c) char burning. In the drying stage, the water from the black liquor evaporates. In the devolatization, the droplet swells, degrades thermally and releases gas phase volatiles such as CO, CO_2, H_2O, NO and light hydrocarbons [31, p. 133]. Subsequently, the combustion of char, a mixture of residual (fixed) carbon and inorganic materials, occurs at char bed situated at furnace floor. When the residual carbon is burned, the inorganic matter forms a molten mixture. It is known as smelt and contains the chemicals to be recovered. The smelt is continuously recovered from the furnace using smelt spouts.

The combustion air system has three levels: primary air, secondary air and tertiary air. The primary and secondary air ports are located below the liquor guns whereas

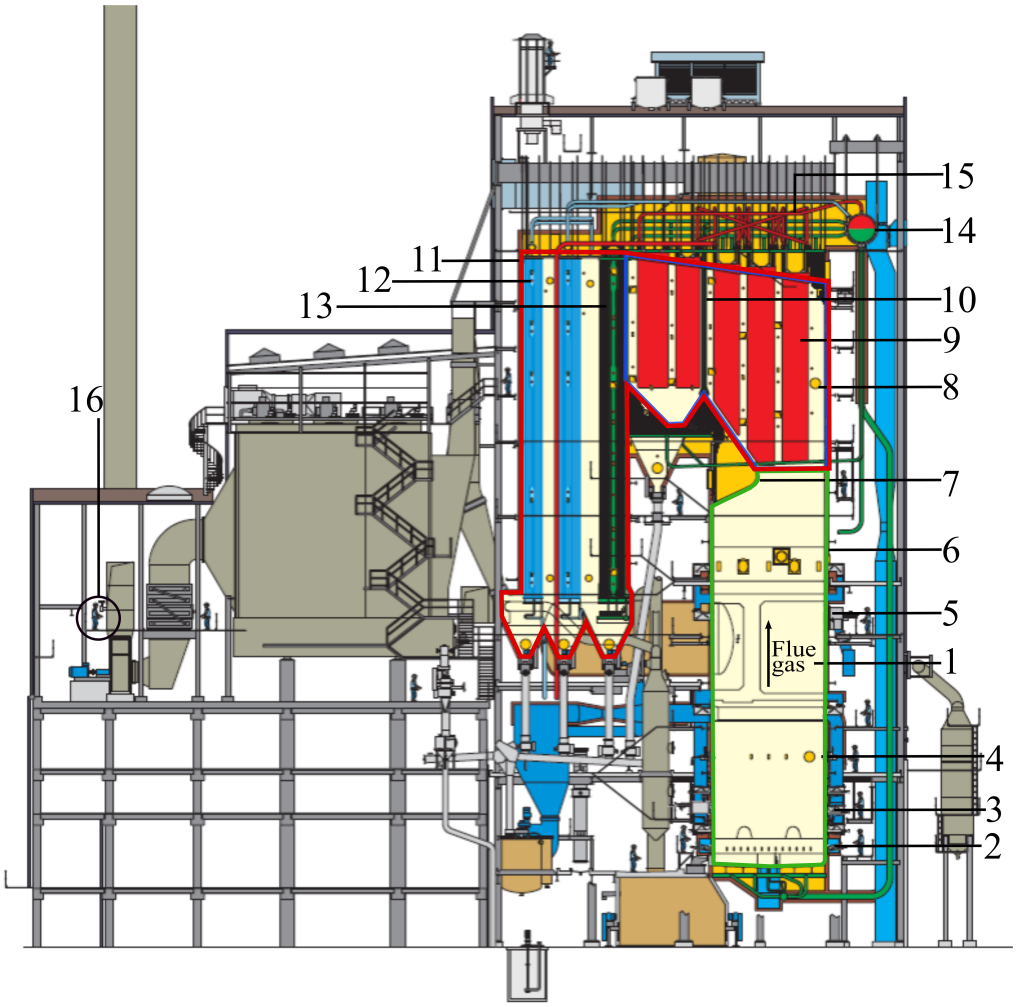

Figure 2.1: A 1000 tds/d capacity recovery boiler (courtesy of Andritz). The main components are: 1) furnace section (marked in green), 2) primary air, 3) secondary air, 4) liquor guns, 5) tertiary air, 6) water walls or boiler walls, 7) nose, 8) superheater region (marked in blue), 9) superheater, 10) rear wall screen, 11) heat transfer section (marked in red), 12) economizer, 13) boiler bank, 14) steam drum, 15) superheaters′ connecting pipes and 16) an operator (for scale).

the tertiary air is located above the liquor guns. Saviharju et al. [32] noted that depending on black liquor dry solids content, about 20-30%, 35-60% and typically 10-40% of total combustion air are introduced at primary, secondary and tertiary levels respectively. The primary air is used to maintain the shape and position of the char bed, and to partially supply combustion air for char gasification. The secondary air controls the height of the char bed and burns the volatiles and gases from char gasification. Finally, the tertiary air supply enables the complete combustion and final mixing of the combustion gases before they enter the heat transfer section. The heat transfer surfaces of the recovery boiler are explained in section 2.3.

2.2 Heat transfer mechanisms

Conduction, convection and radiation contribute to heat transfer to the surfaces in a recovery boiler. These heat transfer mechanisms are explained as follows:

Conduction is the transfer of energy or heat in a medium e.g. solid, liquid and gas due to random motions of molecules known as diffusion [33, p. 68]. It is described by the Fourier's law.

$$q''_{cond} = -\gamma \nabla T \tag{2.1}$$

where, q''_{cond} is the conductive heat flux, γ is the thermal conductivity and ∇T is the temperature gradient across the medium.

In convection, heat is transferred by both bulk motion of the fluids known as advection and conduction [33, p. 378]. It is divided into two types. Forced convection takes place when the flow is induced by external means such as a fan. Natural convection occurs when the flow is caused by buoyancy forces due to a density gradient. Convective heat transfer is mathematically described by the Newton's law of cooling.

$$q''_{conv} = \beta(T_s - T_\infty) \tag{2.2}$$

where, q''_{conv} is the convective heat flux, β is the convective heat transfer coefficient, T_s is the surface temperature and T_∞ is the fluid temperature.

In thermal radiation, the energy is transferred by electromagnetic waves. Unlike conduction and convection, it does not require the presence of a material medium [33, p. 771]. The radiative emissive power of a black body is mathematically represented by the Stefan-Boltzmann law.

$$E_b = \sigma T_s^4 \tag{2.3}$$

where, E_b is the radiative emissive power of a black body, $\sigma = 5.67 \times 10^{-8}$ W/m^{2}K^4 is the Stefan-Boltzmann constant and T_s is the surface temperature.

However, the emissive power of a real body is less than the black body at the same temperature.

$$E = \omega \sigma T_s^4 \tag{2.4}$$

where, E is the radiative emisive power of a real body, ω $(0 \leq \omega \leq 1)$ is known as emissivity. It is a surface property of the real body.

The radiative heat transfer between two bodies e.g. a surface and its surrounding is calculated by

$$q''_{rad} = \omega \sigma (T_s^4 - T_{sur}^4) \tag{2.5}$$

where, q''_{rad} is the radiative heat flux and T_{sur} is the surrounding temperature.

To summarise, the total heat flux (q''_{total}) is calculated as

$$q''_{total} = q''_{conv} + q''_{rad} \tag{2.6}$$

2.3 Heat transfer surfaces

In recovery boilers, both the furnace and convective heat transfer section consist of several heat transfer surfaces with their own functionalities (see Figure 2.1). These surfaces are water preheating surfaces or economizers (12), evaporating surfaces (6, 10 and 13) and superheating surfaces (9). The economizers, superheaters, boiler bank and rear wall screen belong to the convective heat transfer section. All of the heat transfer surfaces are put in an order to achieve the maximum recovery of heat from flue gas and required superheated steam properties including mass flow rate, temperature and pressure [34, p. 1-7].

Natural circulation and boiling process

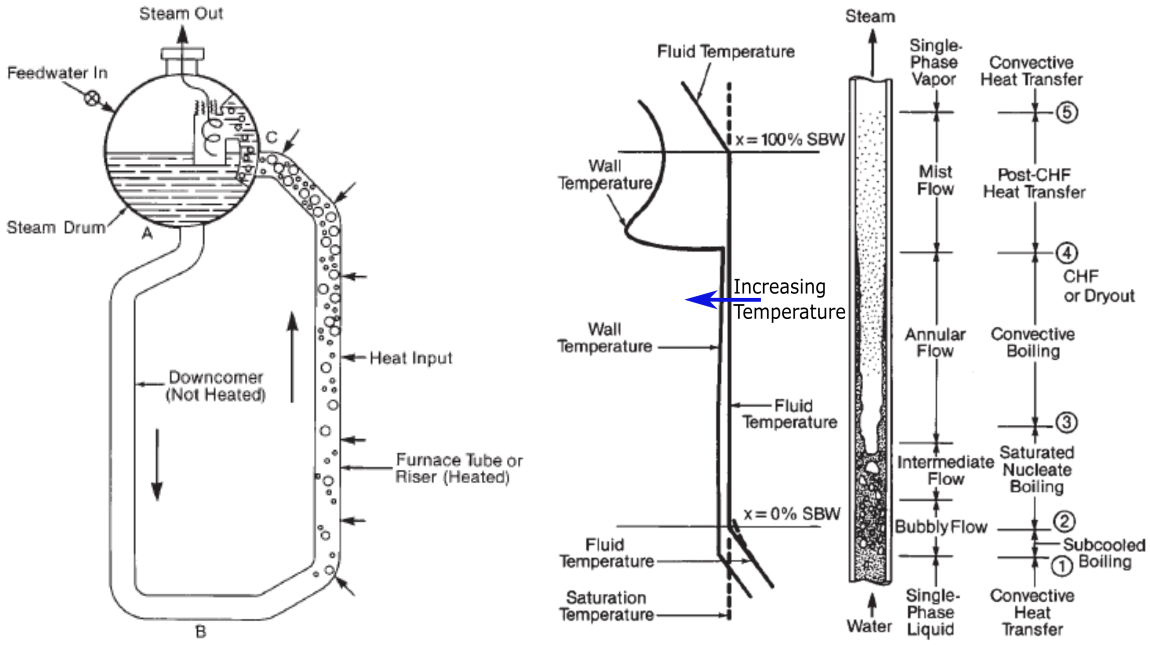

(a) (b)

Figure 2.2: a) Natural circulation in a recovery boiler [34, p. 1-4]. Part AB - unheated downcomer and Part BC- heated riser or evaporating surface. b) Various heat transfer regions and flow regimes in a vertical heated pipe during the evaporation process [34, p. 5-3] and [35].

The water-steam circulation process in recovery boilers is natural circulation (see Figure 2.2a) that is based on the density difference between the preheated water and water-steam mixture.

$$\Delta p = (\rho_{water} - \rho_{mixture}) g \Delta H \tag{2.7}$$

where, Δp is the pressure loss in circulation, ρ_{water} is the density of water, $\rho_{mixture}$ is the density of water-steam mixture, g is the gravitational acceleration and ΔH is the height of circulation [36, p. 6-5].

The steam generation process in recovery boilers is similar to Figure 2.2b and the explanation is based on [34] and [37]. The figure shows the boiling process of preheated water, phase transition and associated flow regimes in a vertical heated pipe. The preheated water is fed into the tube in upward direction. Initially, convective heat transfer heats the preheated water. The preheated water near the tube wall reaches to saturation temperature while the water remains subcooled in the core of the tube. This boiling phenomenon is called subcooled boiling. The transition from subcooled boiling to nucleate boiling occurs when the whole preheated water reaches its saturation temperature. In nucleate boiling, the steam quantity and heat transfer rate increase. The tube wall temperature remains slightly higher than the saturation temperature of water (see Figure 2.2b).

Moreover, various kinds of flow patterns including bubble flow, intermediate flow and annular flow occur during nucleate boiling. These flow patterns are caused by surface tension, interfacial phenomena, pressure drop and water-steam densities [34, p. 5-3]. The bubble flow occurs when the steam fraction is low. The intermediate flow or churn flow consists of large irregular shapes of vapour fragments. This flow regime has a very unstable and chaotic behaviour.

In the annular flow regime, a liquid film forms at the tube wall and the steam with small liquid droplets flows in the core of the tube. Heat is transferred via conduction and convection through the liquid film at the interface of water-steam. This is known as convection boiling. As the liquid film at the tube wall evaporates, dry out occurs and the water-steam flow enters into spray flow regime. The spray flow has mostly saturated steam with a few liquid droplets. The dryout causes rapid increment in tube material temperature that can damage the tube. In the end, all the water droplets, present in water-steam mixture, are evaporated. The heat is then solely transferred to saturated steam via convection and the steam temperature starts to increase (see Figure 2.2b).

In the following, the heat transfer surfaces are explained according to water-steam circulation in recovery boiler. The heat transfer surfaces are shown in Figure 2.3a.

Economizer

The feed water is pumped into the lower header of the economizer (see Figure 2.3b); from where, it starts to flow in upward direction. The economizer is located at the end of the flue gas flow path. The main function of the economizer is to capture the heat from low temperature ($\geq 350^{o}$C) flue gas to preheat the feed water below its saturation temperature by convective heat transfer. A temperature margin, shown in Figure 2.4, is maintained between saturation temperature and preheating temperature to prevent the boiling of feed water and severe damage to the recovery boiler [36, p. 6-3]. The preheated water is collected into the steam drum located at top of the boiler.

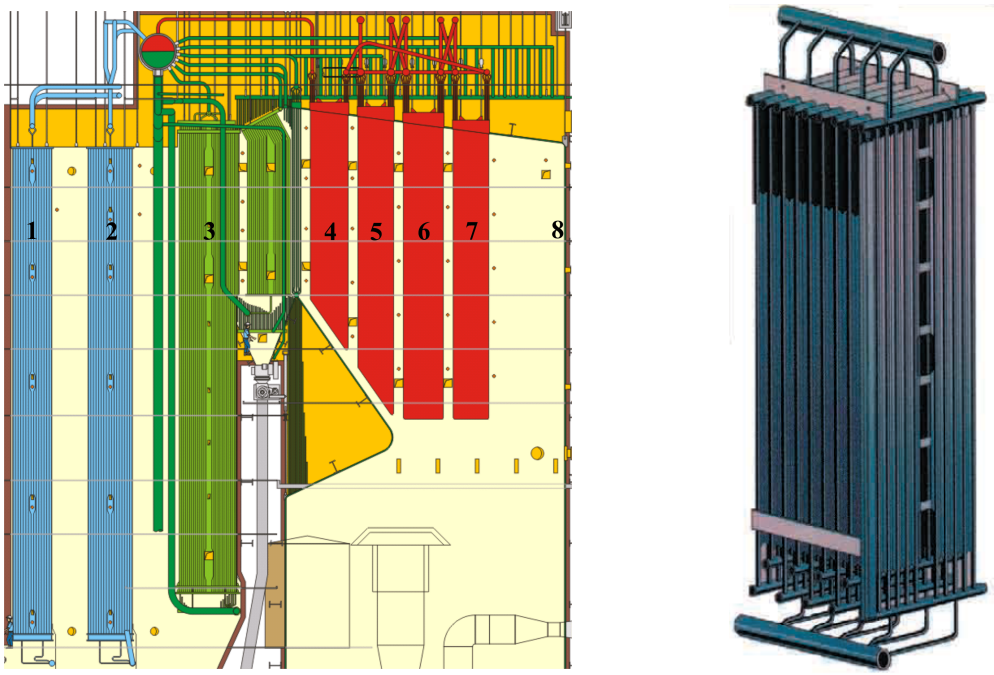

(a) (b)

Figure 2.3: a) Heat transfer surfaces of a recovery boiler (courtesy of Andritz). 1-2) economizers, 3) boiler bank, 4-7) superheaters and 8) boiler walls. b) The economizer [36, p. 6-15].

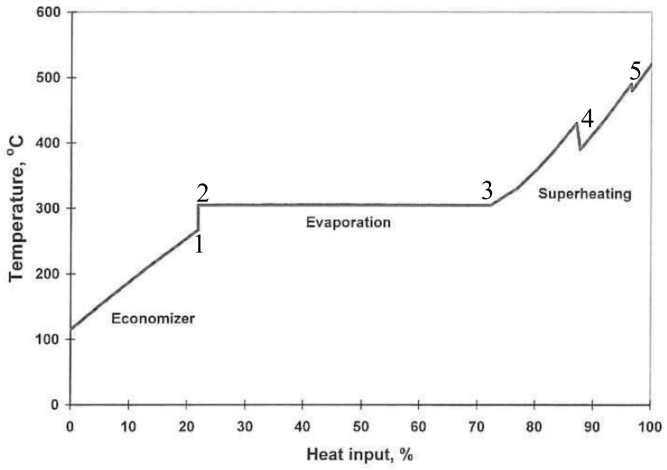

Figure 2.4: Temperature and heat input profile of a recovery boiler. 1-2) maintained temperature margin during economizing. 2-3) phase transition from saturated water to saturated steam during evaporation. 3-5) superheating of saturated steam. The 4 and 5 are the desuperheating stages [36, p. 6-5].

Evaporators

The preheated water from steam drum is fed into the evaporating surfaces including water walls, boiler bank and sometimes screen tubes using downcomers (see Figure 2.5). The water walls receive heat mainly from radiation whereas the boiler bank receives heat mainly from convection. In the evaporation process, phase change occurs and saturated water is converted into saturated steam at almost a constant saturation temperature (see Figure 2.4) [34, p. 1-2] and [36, p. 6-3]. Along with steam generation, the water walls in the furnace section also help to cool the flue gas before it enters into the convective heat transfer section. The reduction in the flue gas temperature helps to prevent particle deposition on the convective heat transfer surfaces and maintain the material temperature of these tube bundles in an acceptable limit for safe boiler operation [34, p. 1-7].

The steam quality at the end of evaporation process is maintained around 50%-60%, similar to the annular flow region described in Figure 2.2b, to avoid dryout and sudden break down of recovery boiler operation. The water-steam mixture is sent back to steam drum where steam is separated from the mixture. The water is further recirculated in the evaporators.

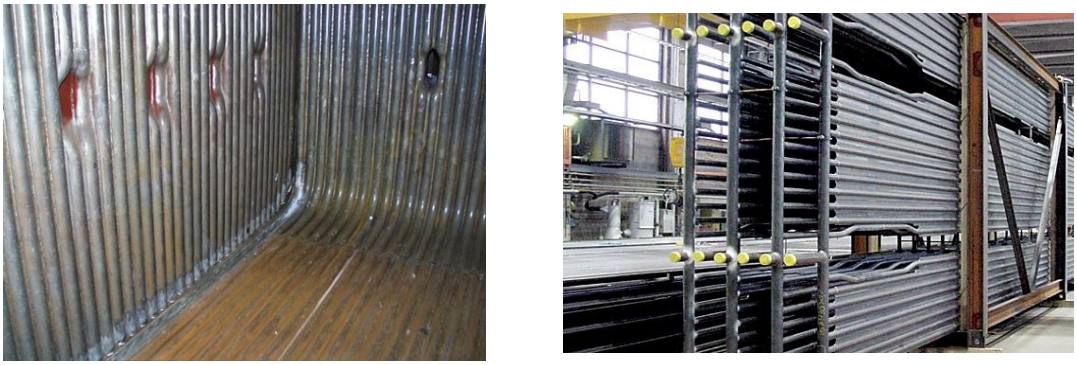

(a) (b)

Figure 2.5: a) Boiler walls in furnace section. b) Boiler bank platens. (Courtesy of Andritz).

Superheaters

The saturated steam separated in the steam drum is further heated until it reaches the final superheat temperature in the superheaters (see Figure 2.6). Water can be injected during superheating to control the main or outlet steam and material temperatures. It is known as desuperheating (see Figure 2.4). The superheaters in recovery boilers are single phase counter-current and co-current heat exchangers. Depending upon the capacity and required outlet steam properties, a recovery boiler may comprise of four to six superheaters [36, p. 6-2]. The superheaters are usually connected in a carefully designed way to control the steam outlet temperature, pressure and also keep the tube material temperature in the acceptable limits [34, p. 1-7].

(a)

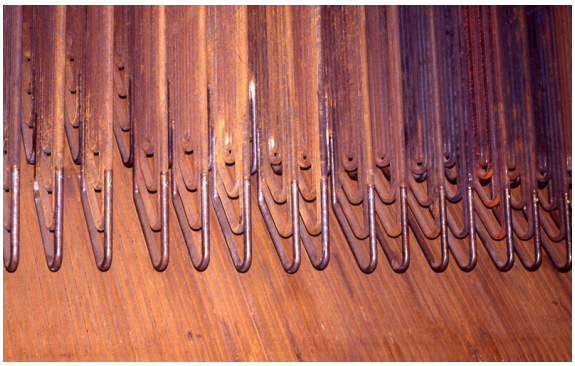

(b)

Figure 2.6: a) Manufactured superheater platens. b) Installed superheater platens across the width of a recovery boiler. (Courtesy of Andritz).

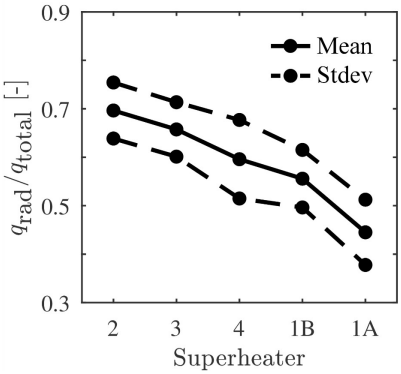

(a)

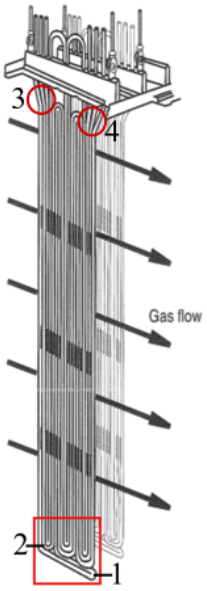

(b)

Figure 2.7: a) The ratio of radiation heat flux to total heat flux for superheaters. The figure has been plotted along the flue gas flow direction in superheater region [29]. b) Flue gas flow between two superheater platens. The longer and shorter flow loops are represented by 1 and 2 respectively. The 3 and 4 represent inlets and outlets for the flow loops [31, p. 13].

Heat transfer in the superheater region (8 in Figure 2.1) is contributed by radiation and convection significantly. For superheaters that are located above the furnace, radiative heat transfer is dominant. Convection is a major heat transfer mechanism in other superheaters. Maakala et al. [29] explained that the ratio of radiation heat flux to total heat flux is higher for the superheaters located just above the nose arch or furnace whereas it is lower for the other superheating surfaces that are located towards the end of the flue gas flow path (see Figures 2.7a).

In modern recovery boilers, each superheater is made of several platens that are equally spaced across the width of the boiler. A platen can be defined as a series of thin in-line tubes with negligible spacing among them. Each tube is a part of an individual flow loop (see Figure 2.7b). A platen may have three to five flow loops. Generally, the flow loops are with different lengths to control the temperature difference among adjacent tubes for safe boiler operation [36, p. 6-12]. A proper platen-wise configuration of superheaters improves the flue gas flow in the superheater region and is also beneficial from deposit removal point of view [31, p. 14].

Chapter 3

Methods and Models

This chapter describes applied methods and developed computational models for integrated CFD/1D-PM simulations for the superheater region in a recovery boiler. The ANSYS Fluent 18.1 and Apros 6 have been used for CFD modelling and 1D-process modelling respectively.

3.1 Description of the case

3.1.1 Description of recovery boiler

Figure 3.1 shows the full geometry of the selected recovery boiler along with the furnace (1), superheater region (2) and inlet (3) for the present work. The capacity of the recovery boiler is 1000 tds/d. The combustion of black liquor in the furnace is assumed to be completed before the flue gas reaches the superheater region, which is the focus of the present work. Therefore, the furnace is not considered in this work. However, the inlet values for the superheater region were obtained from a previously performed furnace simulation. The main operating values for the boiler are shown in Table 3.1. The reference data for the recovery boiler is obtained at about 80% of its total capacity. It comprises of mass and energy balance calculations, and data from the measurement campaign.

Table 3.1: The main operating values for the chosen recovery boiler. All the black liquor values are virgin dry solid values.

Parameters	Values
Boiler type	Kraft recovery boiler
Black liquor capacity, tds/d	1000
Black liquor HHV, MJ/(kgds)	15
BLDS, %	74
Main steam flow, kg/s	49.04
Main steam temperature, ^{o}C	505
Main steam pressure, bar	110

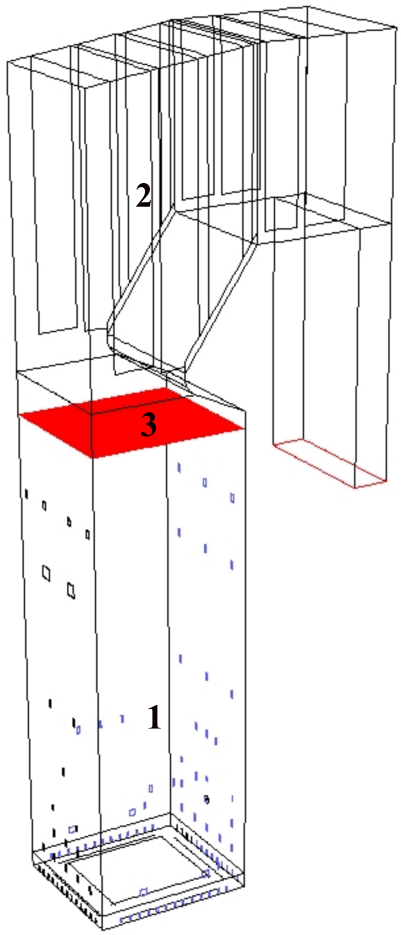

Figure 3.1: The complete geometry of the recovery boiler. 1) furnace, 2) superheater region and 3) inlet for the present computational domain.

3.1.2 Geometry

Figure 3.2a shows a two-dimensional view of the chosen recovery boiler geometry. The ANSYS SpaceClaim is used for geometry creation [38]. The front view, shown in the figure, helps to understand the geometry in a less burdensome way. The important components of the boiler are marked in this figure and its major dimensions are shown in Figure 3.2b.

The inlet (2) is located well above the tertiary level (tertiary air supply) and well below from the nose arch (5) as shown in Figure 3.2a to assure that the tertiary air supply has minimum effect on the flue gas flow and the flow field is steady when flue gas reaches to the superheater region. Similarly, the outlet is located far away from the superheater region to prevent the impact of outlet boundary conditions to the numerical solution of superheater region.

Moreover, the evaporating surfaces including the boiler walls, rear wall screen and boiler bank are also shown in Figure 3.2a. As mentioned in section 2.3, these surfaces are used to generate saturated steam from saturated water at almost a constant

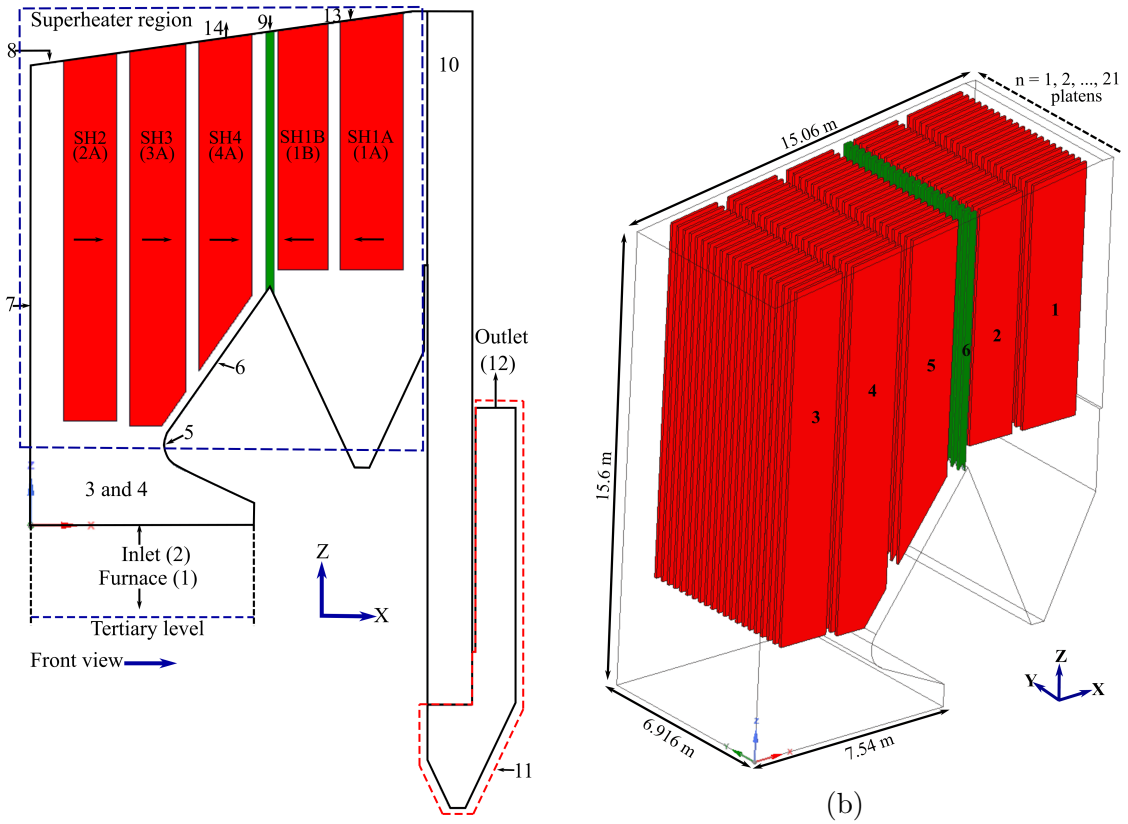

Figure 3.2: a) A two-dimensional view of recovery boiler geometry. 1) furnace (not considered in this work), 2) inlet, 3) right wall, 4) left wall, 5) nose arch, 6) rear wall, 7) front wall, 8) roof or upper wall, 9) rear wall screen, 10) boiler bank region, 11) outlet region, 12) outlet, 13) steam inlet and 14) superheated steam to steam turbine. The superheaters are SH1A, SH1B, SH2, SH3 and SH4. b) An isometric view of recovery boiler and its superheater region. 1) SH1A platens, 2) SH1B platens, 3) SH2 platens, 4) SH3 platens, 5) SH4 platens and 6) rear wall screen platens.

saturation temperature (see Figure 2.4). The boiler walls are right wall (3), left wall (4), rear wall (6), front wall (7) and upper wall or boiler roof (8). In reality, the boiler walls are made of tightly fitted tubes known as heated riser tubes. However, the parts of boiler walls in outlet region (11) are not made of heated risers. Hence, the boiler walls in outlet region do not participate in heat transfer. The boiler bank (10) has platen-wise construction where the platens are equally and tightly spaced across the width of the boiler to increase the heat transfer area for evaporating process. However, in this work, the boiler walls are assumed as flat surfaces and boiler bank is considered as porous medium to reduce the calculation time and complexity of the simulation. The rear wall screen (9) is also a platen-wise evaporating surface and comprises of 21 platens (see 6 in Figure 3.2b).

Furthermore, the superheater region, focus of this work, is shown by a rectangular

box in Figure 3.2a. The chosen recovery boiler has four stages of superheating to produce final superheated steam. The first stage superheaters including SH1A and SH1B are single phase counter-current superheaters according to the flue gas flow direction. They are located towards the end of flue gas flow path. The second stage (SH2), third stage (SH3) and forth stage (SH4) superheaters are single phase co-current or parallel heat exchangers. The superheaters are connected to each other using their inlet headers and outlet headers in the following sequence: steam drum, SH1A, SH1B, SH2, SH3 and SH4. The final superheated steam from SH4 is sent to steam turbine (14) using main steam pipe.

Figure 3.2b shows three-dimensional view of recovery boiler geometry and the platen-wise arrangement of superheaters. Each superheater comprises of 21 platens that are equally spaced across the width of the boiler (in Y-direction). Each platen has in-line thin, seamless and tightly spaced tubes that carry steam inside. In this work, the platens are considered as flat plates and coupled with the 1D-PM of their steam cycle.

3.1.3 Meshing

Figure 3.3 shows a detailed view of computational grid that is discretized using polyhedral cells. Due to the complex geometry and large dimensions, it is very challenging to mesh the computational domain with structured meshing approaches such as hexahedral mesh. Similarly, the tetrahedral mesh increases the overall computational cell count by 3-5 times [39]. Therefore, the polyhedral meshing approach is considered appropriate to discretize the current domain. The ANSYS Fluent Meshing is used for grid generation [40]. The shared topology method is applied to create a conformal mesh at the intersections of superheater region, boiler bank and outlet region. The intersections are represented as P1 and P2 in Figure 3.3. The conformal mesh reduces overall cell counts for the domain and also helps to increase the simulation accuracy.

First, a triangular surface mesh is generated using scoped size functions provided by ANSYS Fluent Meshing. The base size of 38 mm is selected for all the superheater platens and rear wall screen platens to generate uniform triangular surface mesh. Whereas, the base size for other surfaces is 100-150 mm and the growth rate is 1.2. The quality of surface mesh is measured using equilateral volume skewness and inverse orthogonal quality. The triangular surface mesh is then extended to create the polyhedral cells. The cell sizing for polyhedral meshing is based on predefined triangular surface mesh sizing.

The selection of these base sizes is based on following considerations:

1. For superheater platens, the discretization in flue gas flow direction (X-direction) should be dense enough and cell size should be smaller than the superheater tube outer diameter. It is done to assure that the calculation nodes of an individual superheater tube in 1D-PM can precisely map or connect with certain number of faces on the wall of a particular superheater platen. The calculation

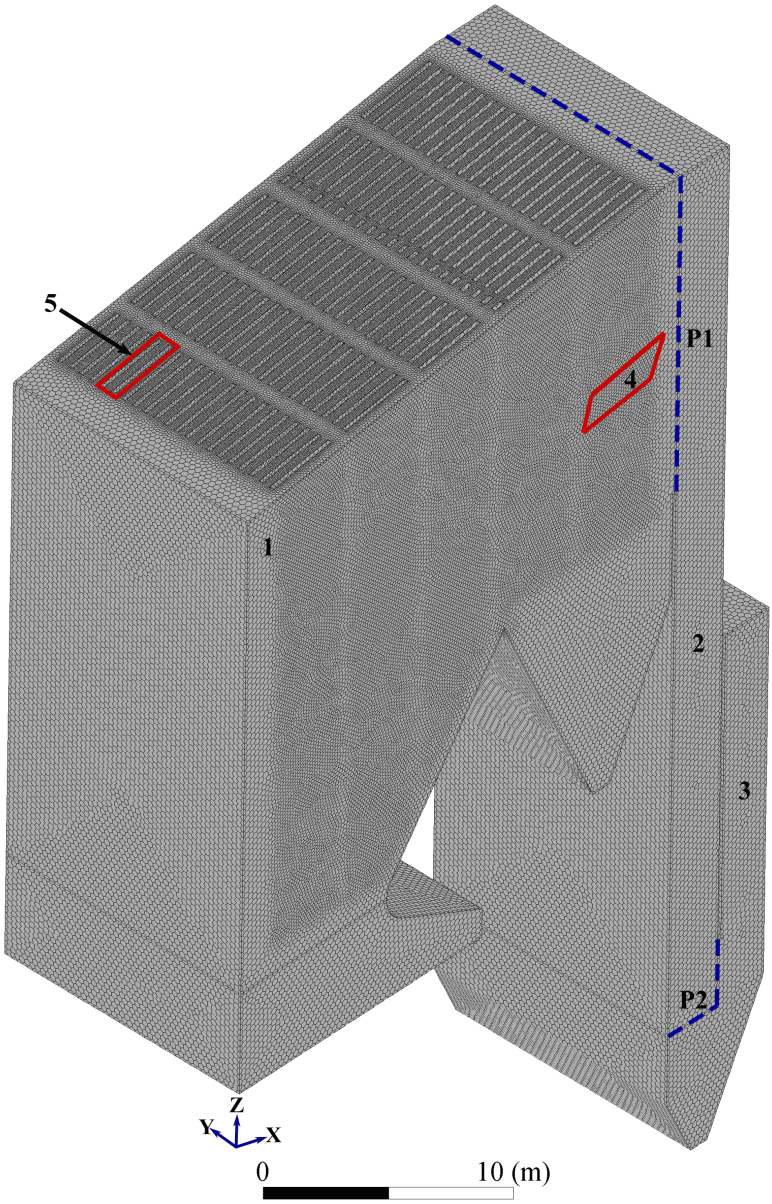

Figure 3.3: An isometric view of computational domain. 1) superheater region, 2) boiler bank, 3) outlet region, 4) SH1A cross-section (detailed view is in Figure 3.4) and 5) flue gas flow path between two SH2 platens (detailed view is in Figure 3.5). The P1 and P2 are the intersections.

nodes are referred to discretization of superheater tubes in 1D-PM. Figure 3.4 shows the generated polyhedral mesh on the wall of a SH1A platen. It can be seen that the calculation nodes of 1D-PM are precisely mapped with a number of faces. The proper mapping of calculation nodes and faces is essential from efficient integrated CFD/1D-PM simulations point of view.

2. The adequate number of cells should present between superheater platens, and

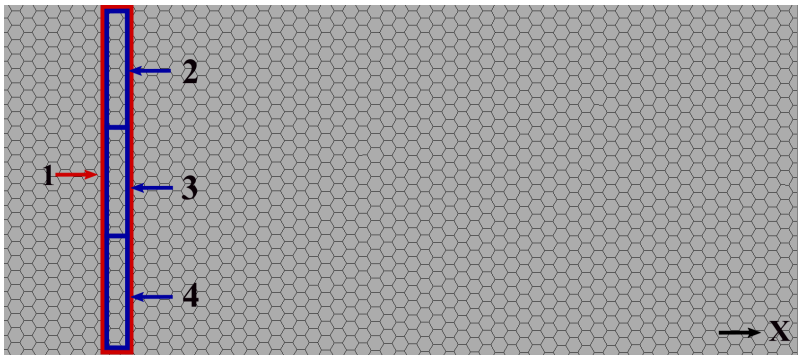

Figure 3.4: Discretization of a SH1A platen wall using polyhedral cells. Only one superheater tube is shown here. 1) superheater tube, and 2, 3 and 4) calculation nodes of superheater tube in 1D-PM. The representative cross-section is marked as 4 in Figure 3.3.

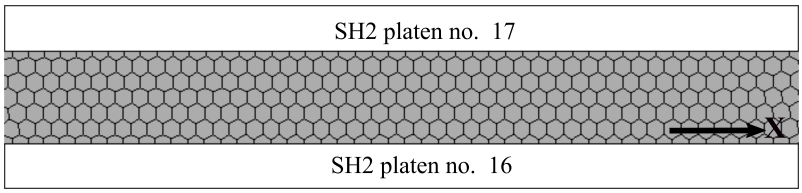

Figure 3.5: The two-dimensional view of discretization between two SH2 platens. The location is marked as 5 in Figure 3.3.

boiler bank region that is modelled as porous medium to accurately solve the flue gas flow field and heat transfer phenomena. An example of computational grid between two SH2 platens is shown in Figure 3.5.

3. Available computational time and computational resources.

The present computational domain has about 13M polyhedral cells. The quality of generated mesh is measured by squish index, ortho skew and aspect ratio as they are the best quality measures for polyhedral mesh [39]. The range for squish index and ortho skew is 0 - 1, where value 0 represents excellent quality of mesh and value 1 shows the mesh with worst quality [39]. The aspect ratio should be less than 35:1 [39]. Table 3.2 shows the calculated values for these quality measures and it can be seen that the generated polyhedral mesh is of a very good quality.

Table 3.2: Quality measures for generated polyhedral mesh.

Quality measures	Minimum value	Maximum value	Average value
Squish index	0.00106	0.795	0.038
Ortho skew	0.00109	0.795	0.04
Aspect ratio	1.32	11.28	2.04

In this work, the grid convergence study is not performed due to the complex geometry and large dimensions of recovery boiler, intricacies due to integrated modelling approach, and available computational time. However, it is noticed from

the literature review that the current computational grid is of finer resolution than previous recovery boiler simulations (Saviharju et al. [23] and Leppänen et al. [24, 25, 26, 27]). In these studies, the calculated results showed reasonable accuracy with the measurements. On the other hand, the current generated mesh is in the range of work done by Maakala et al. [29], in which the results fitted well with measurements.

3.2 CFD modelling for superheater region

The present CFD model solves the fundamental equations of fluid dynamics, turbulence, species transport and radiation in steady-state, Reynolds-averaged form and incompressible flow conditions. The pressure based solver is used and segregated SIMPLE scheme is applied for the pressure-velocity coupling. In the following, the modelling approach is explained in detail. The equations are taken from [29] and [39].

3.2.1 Governing equations and modelling approach

Fluid dynamical equations

The fundamental equations of fluid dynamics are conservation of mass, conservation of momentum and conservation of energy. The conservation of mass is given by continuity equation that is

$$\frac{\partial}{\partial x_j}(\rho u_j) = 0 \tag{3.1}$$

where, ρ is the fluid density and u is the fluid velocity [29].

The conservation of momentum is described by the Navier-Stokes equations.

$$\frac{\partial}{\partial x_j}(\rho u_j u_i) = -\frac{\partial p}{\partial x_i} + \frac{\partial}{\partial x_j}\left[\mu_{eff}\left(\frac{\partial u_i}{\partial x_j} + \frac{\partial u_j}{\partial x_i}\right)\right] - \frac{2}{3}\frac{\partial}{\partial x_i}(\rho k) + \rho g + F \tag{3.2}$$

for i= 1, 2, 3.

where, p is the pressure, μ_{eff} is the effective viscosity, k is the turbulent kinetic energy, g is the gravitational acceleration and F represents other body forces [29]. The conservation of energy is given by energy equation that is described in the following.

Turbulence modelling

The flue gas flow in the recovery boilers is highly turbulent. For instance, the Reynolds number (Re) at inlet of the present computational domain is around 175,000. Therefore, the standard $k-\varepsilon$ model along with standard wall functions is utilized to model the turbulence. This model was developed by Launder et al. [41]

and has been widely adopted for industrial applications since 1972. The standard $k-\varepsilon$ model solves the Reynolds-Averaged Navier-Stokes (RANS) equations along with two separate transport equations for turbulent kinetic energy (k) and its dissipation rate (ε). The transport equations for k and ε are as follows:

Turbulent kinetic energy (k)

$$\frac{\partial}{\partial x_i}(\rho k u_i) = \frac{\partial}{\partial x_j}\left[\left(\mu + \frac{\mu_t}{\sigma_k}\right)\frac{\partial k}{\partial x_j}\right] + G_k + G_b - \rho\varepsilon - Y_M \tag{3.3}$$

for i= 1, 2, 3.

Turbulence dissipation rate (ε)

$$\frac{\partial}{\partial x_i}(\rho \varepsilon u_i) = \frac{\partial}{\partial x_j}\left[\left(\mu + \frac{\mu_t}{\sigma_\varepsilon}\right)\frac{\partial \varepsilon}{\partial x_j}\right] + C_{1\varepsilon}\frac{\varepsilon}{k}(G_k + C_{3\varepsilon}G_b) - C_{2\varepsilon}\rho\frac{\varepsilon^2}{k} \tag{3.4}$$

for i = 1, 2, 3

where, μ_t is turbulent or eddy viscosity, σ_k and σ_ε are turbulent Prandtl numbers for k and ε respectively, G_k and G_b are the generation of turbulent kinetic energy due to mean velocity gradients and due to buoyancy respectively, Y_M is the contribution of the fluctuating dilation in compressible turbulence to dissipation rate, and $C_{1\varepsilon}$, $C_{2\varepsilon}$ and $C_{3\varepsilon}$ are the constants [39].

The turbulent or eddy viscosity is given as

$$\mu_t = \rho C_\mu \frac{k^2}{\varepsilon} \tag{3.5}$$

The values of model constants are $C_{1\varepsilon} = 1.44$, $C_{2\varepsilon} = 1.92$, $C_\mu = 0.09$, $\sigma_k = 1.0$ and $\sigma_\varepsilon = 1.3$ [39].

Flue gas species transport

The flue gas consists of H_2O, CO_2, O_2 and N_2. The transport equation for these species depends on their mass fractions (Y_i) and diffusion fluxes (J_i) . The transport equation is defined as

$$\nabla \cdot (\rho u Y_i) = -\nabla \cdot J_i + R_i \tag{3.6}$$

for i= 1, 2, 3, 4.....N species

where, R_i is the production rate of species by chemical reactions [39]. It is assumed that the combustion of black liquor is finished before the flue gas reaches the superheater region. Therfore, the species production from chemical reactions (R_i) is not considered in this work. In fact, the similar approach has also been applied by researchers such as Saviharju et al. [23] and Maakala et al. [28, 29]. For turbulent flows, the diffusion flux (J_i) of species is given as

$$J_i = -\left(\rho D_{i,m} + \frac{\mu_t}{Sc_t}\right)\nabla Y_i - D_{T,i}\frac{\nabla T}{T} \tag{3.7}$$

where, $D_{i,m}$ is mass diffusion coefficient and $D_{T,i}$ is thermal diffusion coefficient for the species. The $Sc_t = 0.7$ is the turbulent Schmidt number [39].

In the present modelling approach, the mass fractions of H_2O (Y_{H_2O}), CO_2 (Y_{CO_2}) and O_2 (Y_{O_2}) are provided and mass fraction for N_2 (Y_{N_2}) is calculated as

$$Y_{N_2} = 1 - Y_{H_2O} - Y_{CO_2} - Y_{O_2} \tag{3.8}$$

The flue gas properties are based on following laws [39]:

1. The flue gas density is defined as the function of temperature using ideal gas law in incompressible conditions.
2. The specific heat (c_p) is calculated as a function of flue gas composition using mixing-law.
3. The mass-weighted-mixing-laws are used to calculate the viscosity and thermal conductivity.

Energy equation

The energy equation is

$$\nabla \cdot (u(\rho E + p)) = \nabla \cdot \left(\gamma_{eff} \nabla T - \sum_{i=1}^{N} h_i J_i + (\tau_{eff} \cdot u) \right) + S_{rad} \tag{3.9}$$

where, E is internal energy, γ_{eff} is effective thermal conductivity that is $\gamma_{eff} = \gamma + \gamma_t$, γ_t is turbulent thermal conductiviy, h_i enthalpy of the species, τ_{eff} is stress tensor and S_{rad} is radiation source term [39].

Radiation modelling

The radiation source term (S_{rad}) in energy equation (3.9) is solved by radiative transfer equation (RTE) using Discrete Ordinates radiation model. The RTE equation is

$$\nabla \cdot \left(I_\lambda(\vec{r}, \vec{s})\vec{s} \right) + (a_\lambda + \sigma_s) I_\lambda(\vec{r}, \vec{s}) = a_\lambda n^2 I_{b\lambda} + \frac{\sigma_s}{4\pi} \int_0^{4\pi} I_\lambda(\vec{r}, \vec{s}\,') \phi(\vec{s} \cdot \vec{s}\,') d\Omega\,' \tag{3.10}$$

where, I is radiation intensity, λ is wavelength, $\vec{r}$ is position vector, $\vec{s}$ is direction vector, a_λ is absorption coefficient, σ_s is scattering coefficient, n is refractive index, $I_{b\lambda}$ is the black body intensity, ϕ is phase function and $\Omega\,'$ is solid angle [39].

The flue gas species N_2 and O_2 are diathermanous in nature and do not contribute in the radiation. Whereas, the CO_2 and H_2O emit and absorb the radiation at small wavelength bands [42, p. 979]. Therefore, the radiation intensity (I) and absorption coefficient (a_λ) are functions of wavelength. Hence, the non-gray weighted sum of gray gases (WSGG) method with five wavelength bands is implemented with Discrete Ordinates radiation model using user-defined function (UDF). It is based on work done by Dorigon et al. [43].

In addition, the fume particles in recovery boiler affect the radiative properties of flue gas. Their diameter is in the range of 0.1-1 μm. They account for approximately 0.5-2% of flue gas weight in recovery boilers (Wessel et al. [44]). Due to very small size of fume particles, their effect on absorption coefficient (a_λ) is negligible. However, they significantly affect the radiative scatterting as mentioned by Wessel et al. [44]. Therefore, the effect of fume particles on scattering coefficient (σ_s) is also considered by a model based on Wessel et al.[44] and assuming their diameter of 1 μm.

Porous media modelling for boiler bank

The boiler bank region (see 10 in Figure 3.2a) is modelled as porous medium with predetermined porosity, inertial loss coefficients and volumetric heat sink values. The porosity of the boiler bank is calculated using

$$P = \frac{V_{fluid}}{V_{solid} + V_{fluid}} \tag{3.11}$$

where, P is the porosity, V_{fluid} is the volume of void space e.g. flue gas and V_{solid} is the volume acquired by solid components.

The pressure loss (Δp) in porous media is calculated as

$$\Delta p = \zeta n_{row} \frac{\rho u^2}{2} \tag{3.12}$$

where, ζ is inertial loss coefficient and n_{row} is the number of tube rows in flow direction [42]. The inertial loss coefficient is the function of flow velocity in narrowest cross section, Reynolds number, transverse pitch ratio and longitudinal pitch ratio [42, p. 1076]. The calculation for inertial loss coefficient is based on a method described in VDI Heat Atlas [42, p. 1077]. It is provided to ANSYS Fluent as per unit thickness (1/m) in X, Y and Z directions as ζ_x, ζ_y and ζ_z respectively. The volumetric heat sink value is based on reference data. Table 3.3 shows the porosity, volumetric heat sink and inertial loss coefficients for boiler bank.

Table 3.3: Porosity, volumetric heat sink and inertial loss coefficients for boiler bank.

Parameters	Values
Porosity	0.48
Volumetric heat sink, W/m^3	-21983
Inertial loss coefficient, 1/m	
ζ_x	0.88
ζ_y	3.83
ζ_z	0.88

3.2.2 Boundary conditions

Inlet and outlet boundary conditions

The boundary conditions at the inlet (3 in Figure 3.1) are taken from a previously carried out CFD simulation for black liquor combustion in the furnace. The discretization of the furnace is different than the present computational grid. Therefore,

two-dimensional second-degree polynomials, which are fitted using linear regression, are utilized to obtain the inlet boundary condition profiles .

The obtained inlet boundary condition profiles are velocity magnitude and its components in X, Y and Z directions, temperature, turbulent kinetic energy (k), turbulence dissipation rate (ε), and mass fractions of CO_2, H_2O and O_2. The inlet boundary condition profiles are given to ANSYS Fluent using UDF. The mass fraction of N_2 is determined by ANSYS Fluent according to Equation (3.8). Table 3.4 shows the average values for the inlet boundary conditions.

Table 3.4: The average values of the boundary conditions at the model inlet. These values are based on previously performed furnace simulation. The velocity in upward direction (Z-direction) is represented by u_z.

Parameters	Values
Velocity (u), m/s	4.65
u_z, m/s	3.86
Temperature, ^oC	932
Flue gas mass flow rate, kg/s	56.78
Reynolds number (Re)	175,000
Flue gas composition	
Carbon dioxide (CO_2), wt%	21
Gaseous water (H_2O), wt%	15
Oxygen (O_2), wt%	2
Nitrogen (N_2), wt%	62

To scrutinize the accuracy of this approach, the obtained flue gas mass flow rate, temperature and species mass fractions at the inlet (see Table 3.4) were compared with reference data, and a very good agreement was found. However, the accuracy of this approach in context of turbulent kinetic energy (k) and its dissipation rate (ε) is not analysed due to the lack of information.

In addition to this, the pressure outlet boundary condition is selected for the outlet of the computational domain.

Wall boundary conditions

The momentum boundary conditions for all the walls including boiler walls, rear wall screen platens and superheater platens are set to fixed walls and no-slip conditions. The effect of wall roughness on heat transfer to the walls is also considered using the standard wall roughness model provided by ANSYS Fluent. The virtual shifting of the wall approach is applied and roughness parameters including roughness height (K_s) and roughness constant (C_s) are defined. The roughness height (K_s) is set to 19 mm that is the half of cell size defined for discretizing the superheater platens′ walls. The wall roughness constant (C_s) is set to 1 [39].

The thermal boundary conditions to the walls except superheater platens are convective heat transfer boundary conditions. The superheater platens are coupled

with 1D-PM using two-way heat transfer coupling method. The thermal boundary conditions for superheater platens are described in section 3.4.2.

The total heat flux to the wall is

$$q''_{total} = \underbrace{\beta_{gas}(T_w - T_{gas}) + q''_{rad}}_{\text{Flue gas side}} = \underbrace{\beta_{total}(T_{ref} - T_w)}_{\text{Water-steam side}} \tag{3.13}$$

where, β_{gas} is convective heat transfer coefficient towards flue gas side, T_w is wall surface temperature, T_{gas} is flue gas temperature, q''_{rad} is radiative heat flux, β_{total} is overall heat transfer coefficient and T_{ref} is free stream temperature. The overall heat transfer coefficient (β_{total}) and free stream temperature (T_{ref}) are provided to the ANSYS Fluent. The overall heat transfer coefficient is calculated using

$$\beta_{total} = 1/\left(\frac{\delta_{deposit}}{\gamma_{deposit}} + \frac{\delta_{tube}}{\gamma_{tube}} + \frac{1}{\beta_{fluid}}\right) \tag{3.14}$$

where, $\delta_{deposit}$ is deposit thickness on the walls, $\gamma_{deposit}$ deposit thermal conductivity, δ_{tube} is superheater tube thickness, γ_{tube} is superheater tube thermal conductivity and β_{fluid} is water-steam side heat transfer coefficient.

In recovery boilers, the deposit thickness and its thermal conductivity are hard to estimate. The literature review reveals that the deposit thickness in recovery boilers is in range of 5-60 mm and the deposit thermal conductivity is in range of 0.1-2.5 W/(mK) (Leppänen et al. [25], Maakala et al. [29], Li et al. [45] and Zbogar et al. [46]). Due to these uncertainty involved, the overall heat transfer coefficients (β_{total}) were fitted to reference data, similarly as has been done in previous works such as Saviharju et al. [23], Leppänen et al. [25] and Maakala et al. [28, 29]. Table 3.5 shows the deposit thickness, and thermal boundary conditions for boiler walls, boiler bank and rear wall screen.

Table 3.5: Wall thermal boundary conditions. For superheaters, β_{total} and T_{ref} are calculated during integrated CFD/1D-PM simulations.

Walls	β_{total} [W/m^{2}K]	T_{ref} [K]	$\delta_{deposit}$ [mm]
Boiler walls	28.3	599	35
Boiler bank walls	28.3	599	35
Rear wall screen	610	599	1.2
SH1A			1.0
SH1B			3.5
SH2			13.5
SH3			8.0
SH4			6.7

3.3 1D-process modelling for superheater region

3.3.1 Description of steam cycle

Figure 3.6 shows the steam cycle of the superheater region including steam drum, inlet headers, outlet headers and superheater platens from the top view of recovery boiler geometry (see also Figure 3.2b). The water-steam mixture from the evaporating surfaces is collected into the steam drum (1) where the saturated steam is separated from the water-steam mixture and sent to superheaters for increasing its temperature to the required outlet temperature.

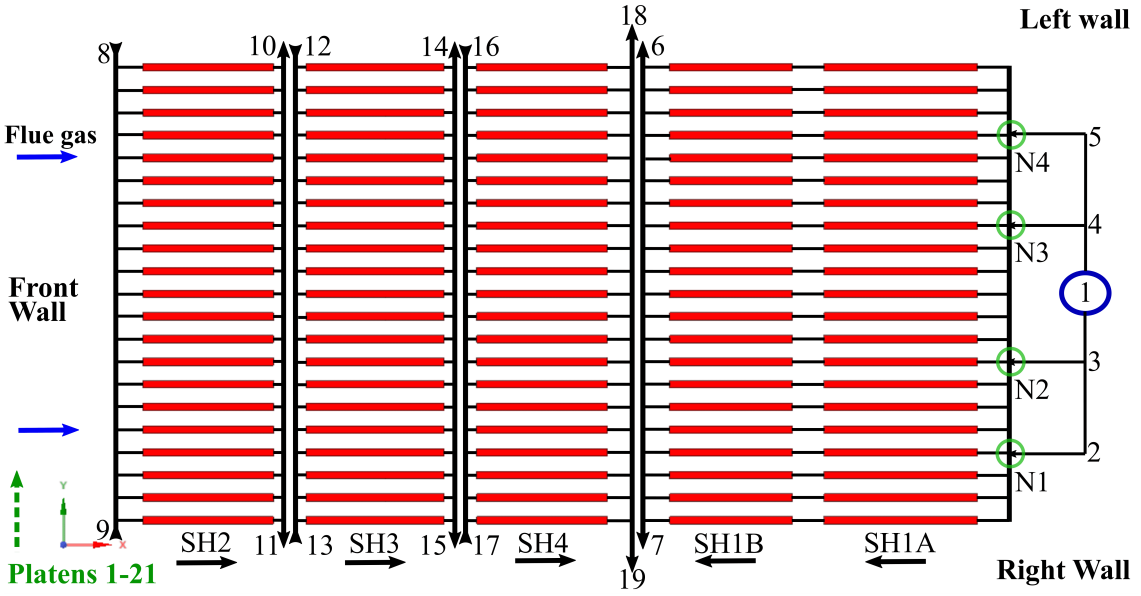

Figure 3.6: The superheater region steam cycle. 1) steam drum, 2, 3, 4, 5) steam drum to SH1A inlet header connecting pipes, 6, 7) SH1B outlet header, 8, 9) SH2 inlet header, 10, 11) SH2 outlet header, 12, 13) SH3 inlet header, 14, 15) SH3 outlet header, 16, 17) SH4 inlet header, and 18, 19) SH4 outlet header. N1, N2, N3 and N4 are the cross-junctions in SH1A inlet header.

The superheated steam generation process starts in a way that the steam drum (1) feeds saturated steam into the inlet header of SH1A ; from where, the steam is distributed among the SH1A platens. The heat transfer between SH1A platens and hot flue gas occurs, and steam temperature starts to increase. Every SH1A platen is directly connected to an individual platen of SH1B. The slightly superheated steam flows from SH1A platens to SH1B platens where its temperature further increases and it is collected into the SH1B outlet header (6-7). The SH1A and SH1B are counter-current heat exchangers and receive heat from hot flue gas mainly from convection.

The steam from SH1B outlet header (6-7) passes to SH2 platens via SH2 inlet header (8-9). The headers are connected in cross-pattern using connecting pipes. For

instance, the SH1B outer header exit 7 is connected to SH2 inlet header at location 8 (see Figure 3.6). The steam has a similar flow pattern when it passes from SH2 to SH3 as well as SH3 to SH4. The superheaters SH2, SH3 and SH4 are parallel flow heat exchangers and receive heat from the hot flue gas through radiation and convection. The final superheated steam from the SH4 is sent to steam turbine using the SH4 outlet header (18-19) and the main steam pipe.

3.3.2 Main flow components

The 1D-PM for superheater region is developed with APROS 6 [47]. It is a dynamic process simulation tool developed by Fortum and VTT Technical Research Centre of Finland Ltd. The 1D-PM comprises of various process components including point, node, pipe, heat pipe, T-junction (TEE) and control valve. These process components are shown in Figure 3.7.

The point (1) and node (2) connect different kind of process components. They are also used to define the X, Y and Z (elevation) coordinates that are essential for performing integrated 3D CFD/1D-PM simulations. However, the point and node have a significant difference from calculations of flow properties point of view. The calculation node of a point receives the volume and area from the components that are connected to it whereas the volume and area of a node are defined by the user for further calculations [47].

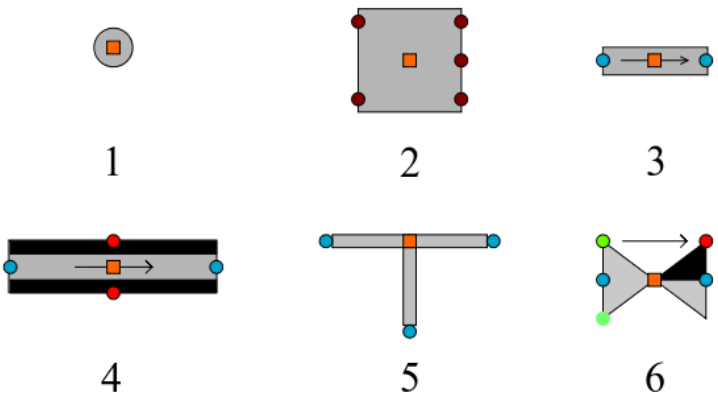

Figure 3.7: The main flow components for 1D-PM. 1) point, 2) node, 3) pipe, 4) heat pipe, 5) T-junction (TEE) and 6) control valve.

In process simulations, the main function of the pipe component (3) is to calculate the fluid flow. Similarly, the heat pipe (4) is utilized to simulate the heat transfer along with fluid flow. Moreover, the T-junction (5) is used to model the right angle (90°) T-junctions for different kind of flow configurations including diverging flow and converging flow [47]. The main function of the control valve (6) is to control

and provide the required fluid flow rate. It calculates the required fluid flow rate by determining the available flow area based on valve position [47].

3.3.3 Modelling approach

Solver

The superheaters have single phase steam flow. Therefore, the thermal-hydraulic properties of steam flow in superheater tubes are solved using homogeneous model or three-equation model [47]. This model solves the conservation equations for mass, momentum and energy for the superheated steam in one direction (Z-direction). The pressure losses in pipe flow are mainly caused by pipe friction and minor losses or form losses due to the geometrical structure of piping system [5, 48]. The total pressure loss in a pipe flow are calculated as

$$\Delta p = \left[f\frac{L}{d} + K_{total} \right] \frac{\rho u^2}{2} \tag{3.15}$$

where, f is the friction factor, L is pipe length, d is inner diameter of pipe and K_{total} is the sum of all form loss coefficients in the piping system.

$$K_{total} = K_1 + K_2 + K_3 ... + K_n \tag{3.16}$$

The friction factor (f) is

$$\frac{1}{\sqrt{f}} = -0.869 ln \left[\frac{\eta/d}{3.7} + \frac{2.523}{Re\sqrt{f}} \right] \tag{3.17}$$

where, η is relative roughness and Re is Reynolds number. The friction factor (f) is obtained from Moody diagram [48]. The form loss coefficients for the 1D-PM are based on Figure 3.8.

Steam drum

The steam drum is a large horizontal cylindrical shape tank comprised of several openings [5]. These openings include incoming preheated water from economizers, downcomers for evaporating surfaces, incoming water-steam mixture from evaporating surfaces and outgoing saturated steam to superheater region. In this work, the main focus is the superheater region. Therefore, the steam drum is modelled as a point by defining the elevation and saturated steam properties including temperature, pressure and void fraction.

Headers

The platens of an individual superheater are connected to the inlet header and outlet header. The inlet header distributes the steam to all the platens whereas the outlet header collects the steam and sends to next stage of superheating or to main steam

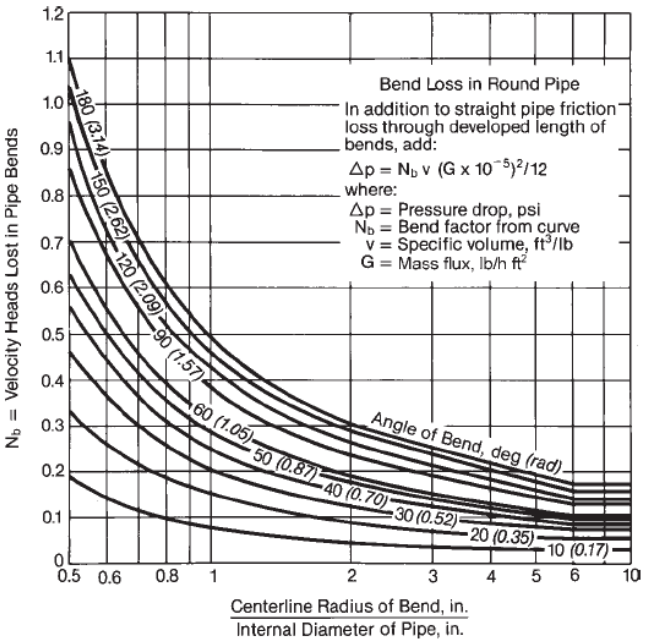

Figure 3.8: The form loss coefficients for circular bends [34, p. 3-14].

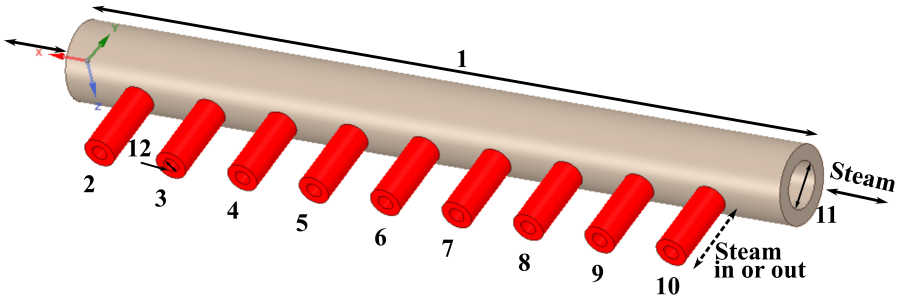

Figure 3.9: The simple geometry of inlet and outlet headers. 1) main header pipe, 2-10) connections to superheater platens, 11) main header pipe diameter and 12) junction pipe diameter.

pipe that is connected to steam turbine. Figure 3.9 describes an example of inlet and outlet headers.

It can be seen in Figure 3.9 that there are 90° T-junctions at the locations where the superheater platens are connected to the header. Figures 3.10b and 3.10c show the superheated steam flow patterns in the inlet header and outlet header along with the major dimensions. Therefore, this kind of geometrical structure in 1D-PM is modelled using T-junction component. The required number of T-junctions are connected in a series using connecting points as shown in Figure 3.10a. The main advantage of using T-junction component is that it dynamically calculates the form

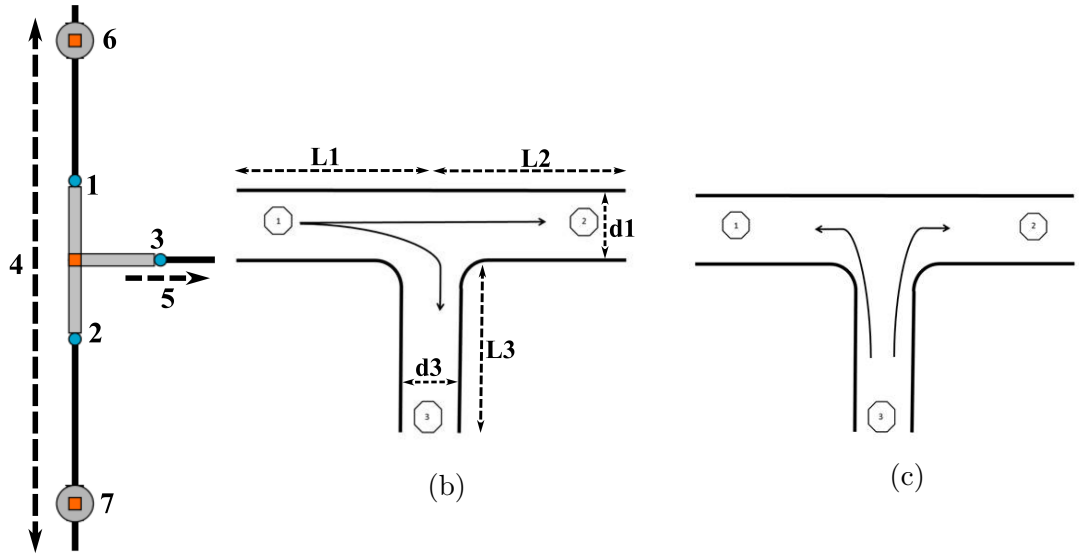

(a) (b) (c)

Figure 3.10: a) The one component of inlet header model in 1D-PM. 1,2 and 3) the branches of T-junction, 4) main header pipe, 5) steam to superheater platen, and 6 and 7) connecting points. b) Superheated steam flow in inlet header. c) Superheated steam flow in outlet header. L1, L2 and L3 are length of branches in Figure 3.10a. The d1 and d3 are the inner diameters of main header pipe and junction pipe respectively [47].

loss coefficients for each of its branches and increases the process simulation accuracy compared to using constant values for form loss coefficients. It was also studied in this work with simulations and seen to give most accurate results in comparison of point and node components in which the form loss coefficients are manually defined. The dynamic calculations used for these form loss coefficients are based on theory given by Rennels and Hudson [47, 49].

In particular to SH1A inlet header, there are four locations where the connecting pipes that carry saturated steam from the steam drum are connected and make cross flow junctions. The locations of these cross-junctions are represented as N1, N2, N3 and N4 in Figure 3.6. The flow pattern at these junctions is shown in Figure 3.11a. These cross-junctions in 1D-PM are modelled using node and pipe components as shown in Figure 3.11b. The calculation for the form loss coefficients for each branch of a cross-junction is based on the ratio of volumetric flow rate in an individual branch to total volumetric flow rate entering the cross junction (Sharp et al. [50]).

Superheater platen

It was mentioned in previous sections that a superheater platen is made of several in-line as well as tightly spaced thin and seamless tubes, and that each tube belongs to a particular superheated steam flow loop. In fact, all the platens of a superheater

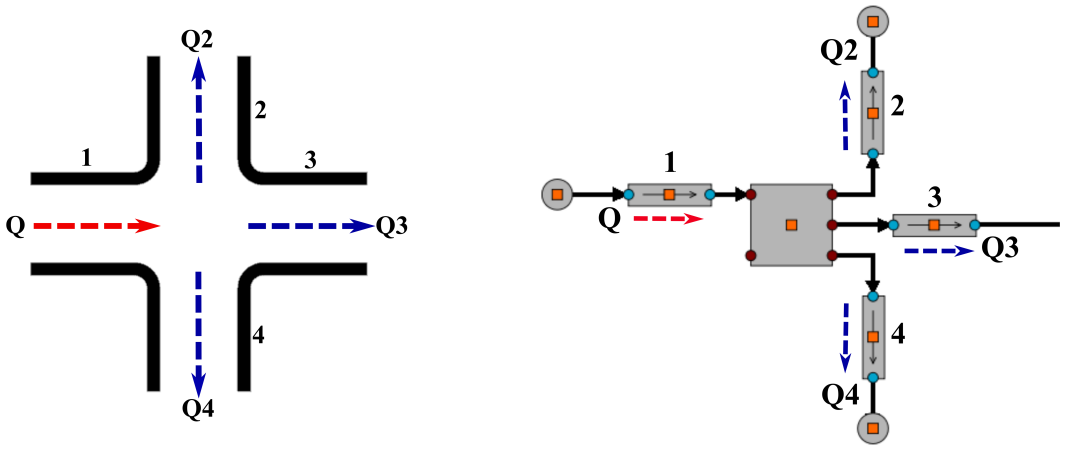

(a) (b)

Figure 3.11: a) Dividing flow scenario at cross-junctions in SH1A inlet header. b) The representative model in 1D-PM. The Q is total volumetric flow rate entering the cross-junction. The Q2, Q3 and Q4 are the volumetric flow rates in branches 2, 3 and 4 respectively.

are identical. In the 1D-PM, the superheater platens are designed using the User Component approach provided by APROS 6. The superheated steam flow loops are modelled using the heat pipe component and point component. The flow loops of SH2 platens are presented in Figure 3.12. The platens of other superheaters have similar kind of flow loop structures where only the number of loops is different. The material properties for superheaters including specific heat (c_p) and thermal conductivity (γ_{tube}) are given for five temperature ranges in the form of second-degree polynomials [47]. The material for deposits on superheater tubes is also defined and shown in Table 3.6 ([31, p. 166]). The deposit thickness values for superheater tubes are described in Table 3.5.

Table 3.6: The properties of deposits and materials for superheaters. T is temperature, and A_1, A_2, A_3, B_1, B_2 and B_3 are the coefficients.

Parameters	Values
Deposition properties	
Density (ρ), kg/m^3	2163
Specific heat (c_p), kJ/kg/K	1.42
Thermal conductivity ($\gamma_{deposit}$), W/mK	1.0
Superheater material properties	
c_p	$A_1 + A_2T + A_3T^2$
γ_{tube}	$B_1 + B_2T + B_3T^2$

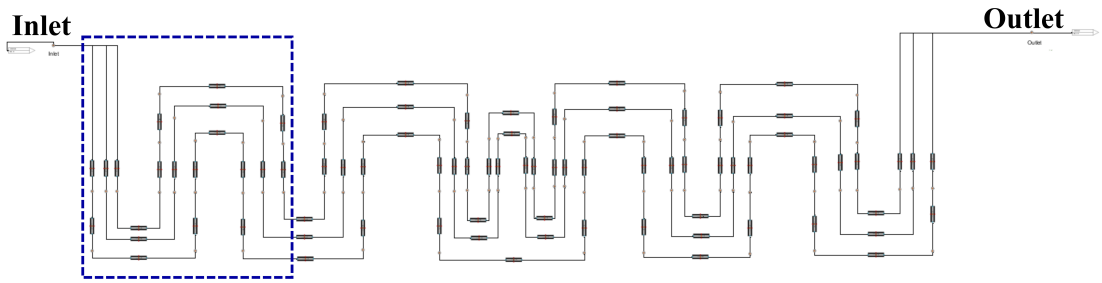

(a)

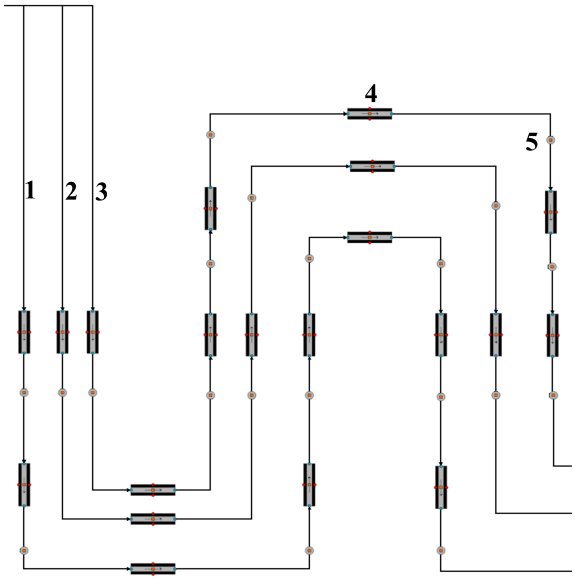

(b)

Figure 3.12: a) The developed 1D flow model for SH2 platens using the User Component approach. b) The detailed view of cross-section marked in Figure 3.12a. 1, 2 and 3) the superheated steam flow loops, 4) heat pipe component and 5) point component.

Desuperheating stages

The superheating process consists of three stages of desuperheatnig where water is injected to control the steam temperature. In the 1D-PM, these stages are modelled using control valves. The properties of injected water during desuperheating stages are shown in Table 3.7

Connecting pipes

The inlet headers and outlet headers of the superheaters are connected to each other in a cross pattern using connecting pipes. The geometrical configurations of these pipes is shown in Figure 3.13. In the 1D-PM, each connecting pipe is modelled as a single pipe component with a total flow length and total form loss coefficient (K_{total}).

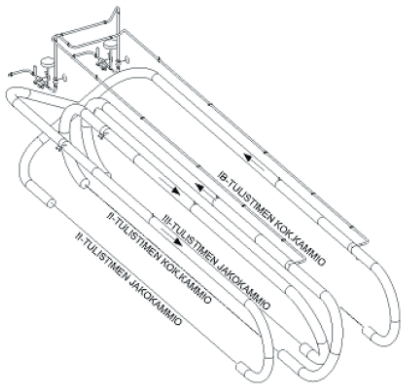

Figure 3.13: The connecting pipes for inlet headers and outlet headers of superheaters [36].

3.3.4 Boundary conditions

The inlet and outlet boundary conditions for the 1D-PM are shown in Table 3.7, they are based on the reference data. The pressure at the outlet is adjusted to obtain a superheated steam mass flow rate similar to the reference data. The thermal boundary conditions for superheater platens are explained in section 3.4.2.

Table 3.7: The boundary conditions for the 1D-PM and properties of injected water during desuperheating stages.

Parameters	p [bar]	T [^oC]	$\dot{m}$ [kg/s]
Inlet	121.9	325.9	
Outlet	Adjusted	506	38.2
Desuperheating stages			
Pressure and temperature values for each stage	124.9	140.5	
SH1-SH2			0.18
SH2-SH3			0.62
SH3-SH4			0.26

3.4 Integrated CFD/1D-PM modelling

The integrated CFD/1D-PM modelling for the superheater region is performed using the coupling feature of APROS 6. In the following, the face and node mapping, exchange parameters and integrated simulation approach are explained in detail.

3.4.1 Node and face mapping

To perform coupled simulations for the flue gas side and steam cycle in the superheater region, it is essential to link the 3D-CFD model with the 1D-PM. The link between

these models is defined by connecting their discretized elements or computational cells at particular locations. This is known as node and face mapping. In the 1D-PM, each superheater tube or heat pipe in the flow loop of a superheater platen is dicretized in 10 elements in Z-direction. The discretized elements are known as calculation nodes of heat pipe. The positions of tubes in the superheater platens are specified by defining the X, Y and Z coordinates of the connecting points. Figures 3.14 and 3.15 show the mapped nodes and faces for integrated CFD/1D-PM simulations.

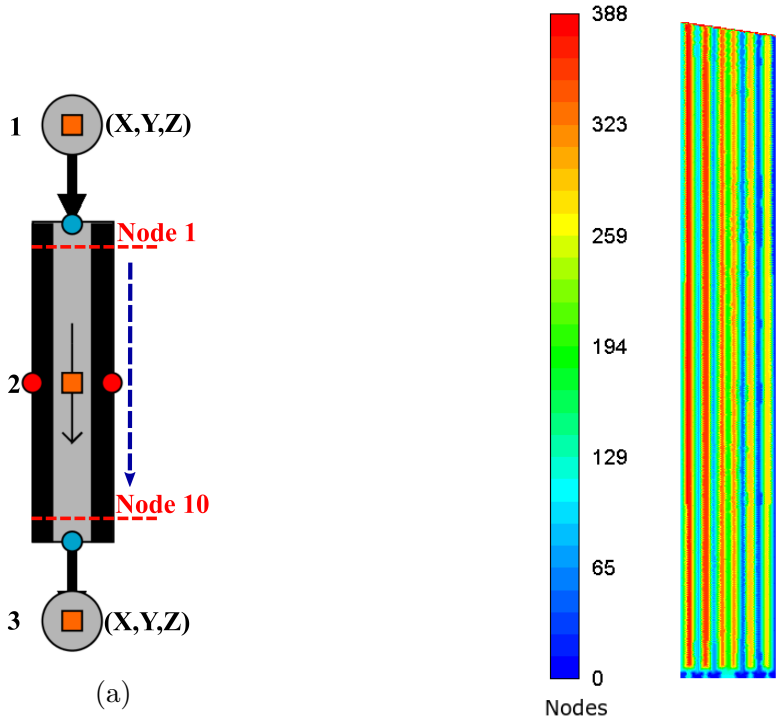

(a) (b)

Figure 3.14: a) Discretization of a superheater tube and coordinates of connecting points. 1 and 3) connecting points and 2) superheater tube. b) Mapping of 1D-PM side dicretization of superheater tubes with CFD side computational cells for a SH2 platen. The legend describes the indices of mapped calculation nodes (heat structure nodes). Therefore, there are 388 nodes in this superheater platen. Indirectly, the figure also shows the superheater tubes.

The coordinates of connecting points are defined as

In X-direction or flue gas flow direction

$$X_i = X_1 + n \times X_p \tag{3.18}$$

and for 90° bends in flow loops

$$X_i = X_1 + n \times X_p \pm R_{arc} \tag{3.19}$$

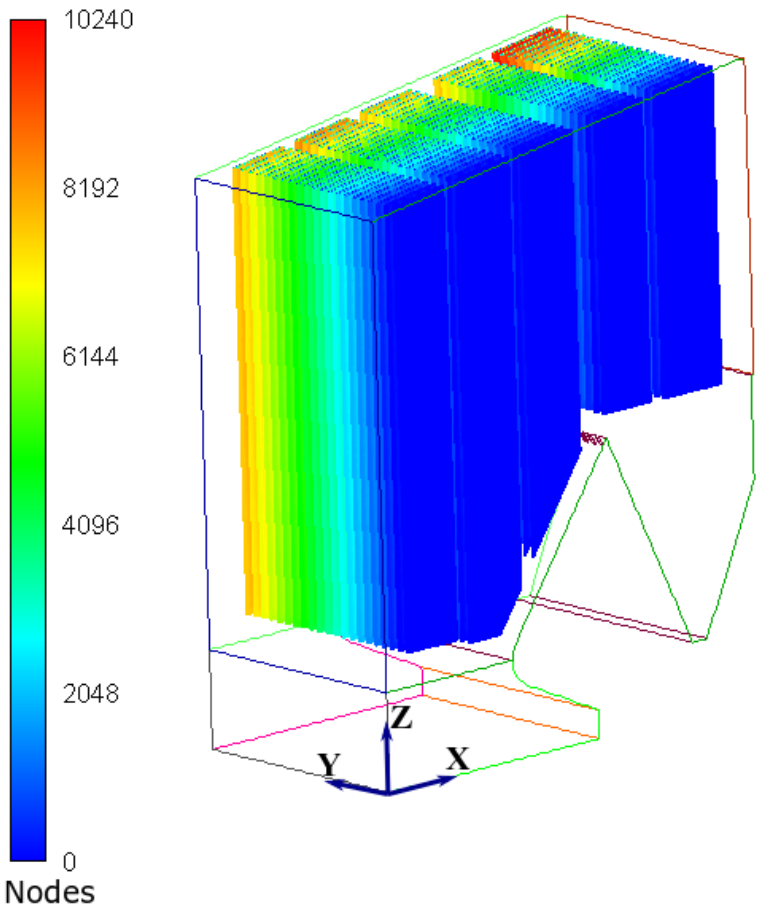

Figure 3.15: The mapped calculation nodes (heat structure nodes) of 1D-PM with CFD side computational cells for superheater platens.

where, X_i is the X coordinate of point, X_1 is the distance of superheater platen inlet from the front wall of the boiler, n is the number of tubes in superheater platens in X direction or flue gas flow direction, X_p is center to center distance between adjacent tubes and R_{arc} is the arc radius of 90° bends.

In Y-direction

$$Y_i = Y_1 + m \times Y_p \tag{3.20}$$

where, Y_i is the Y coordinate of the point, Y_1 is the distance of first superheater platen from the right wall of the boiler, m is the number of platens and Y_p is distance between superheater platens.

In Z-direction

$$Z_i = H \tag{3.21}$$

where, Z_i is the Z coordinate of the point and H is the elevation from the ground.

3.4.2 Boundary conditions exchange

Figure 3.16a represents a superheater tube and describes the thermal boundary conditions for superheater platens during integrated CFD/1D-PM simulations. The heat structure nodes (HN1-HN9) are generated along with the calculation nodes (N01-N03) of the heat pipe. The heat structure nodes calculate the steam temperature, superheater tube material temperature and surface temperature of the deposit layer.

The heat structure nodes of the deposit layers on the superheater tubes are mapped with the faces at specified locations on the walls of the superheater platens in the CFD model. During coupled simulations, APROS 6 calculates the surface temperature (T) at deposit layers and sends it to Fluent. The CFD model then determines the surfaces heat transfer (q) and transfers it to the mapped heat structure nodes. Therefore, it can be said that the thermal boundary conditions for the superheater platens in CFD model are surface temperatures obtained from the 1D-PM.

3.4.3 Integrated simulation approach

During the coupled simulations, Fluent solves the flue gas side in the superheater region in steady state and incompressible conditions. Whereas, the 1D-PM runs only in transient mode which is enforced by the APROS 6. The time step for the 1D-PM is set to 0.1 sec. It was found that the coupling feature of APROS 6 does not work optimally when Fluent simulates the flue gas side in steady state conditions. The problem is that the coupling feature exchanges the boundary conditions at every Fluent iteration instead of exchanging the parameters after defined higher number of iterations i.e. better convergence. This causes the 1D-PM to achieve convergence very slowly and increases the simulation time for the coupled simulations drastically.

A coupling-decoupling strategy was devised and applied to handle this problem and reduce the computational time. It is described in Figure 3.16b. Initially, the CFD and 1D-PM simulations were run in coupled way where the boundary conditions were exchanged once per Fluent iteration. Afterwards, the standalone 1D-PM was used to simulate the superheated steam cycle until it reached convergence. This strategy was utilized for four times before running the final integrated CFD/1D-PM simulations, which resulted in convergence.

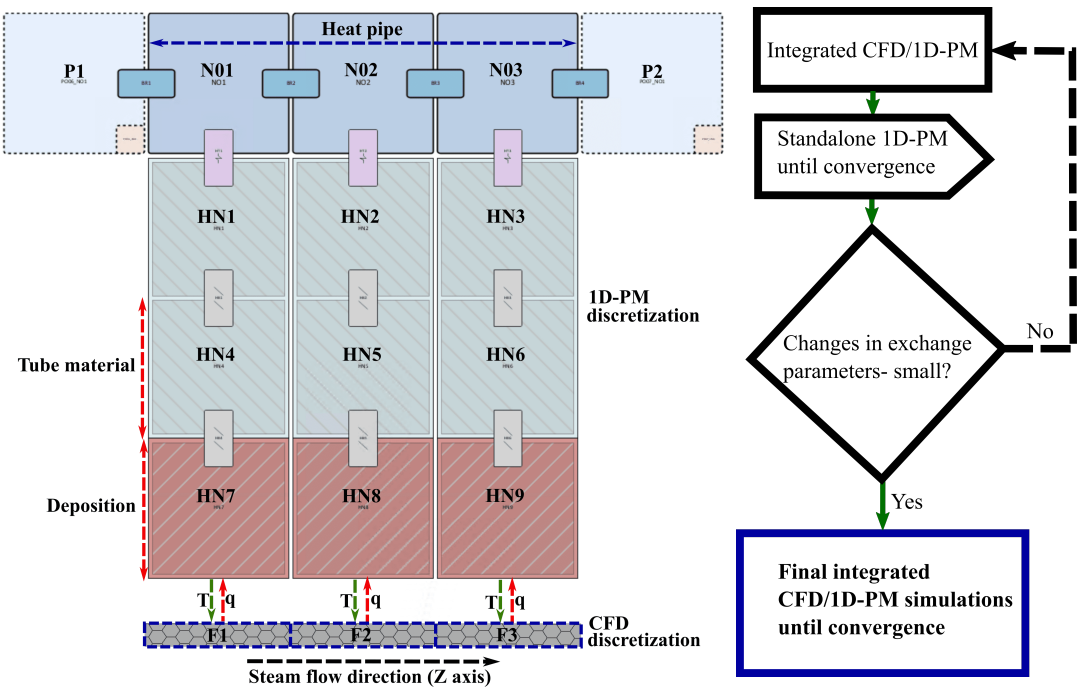

Figure 3.16: a) The exchange parameters during integrated CFD/1D-PM simulations. One superheater tube is presented. The P1 and P2 are the connecting points. N01-N03 are the calculation nodes of heat pipe or superheater tube. HN1-HN3 are the heat structure nodes for steam temperature calculations. HN4- HN9 are the heat structure nodes in tube material and deposit layer for material temperature calculations. F1-F3 are the coupled faces for the tube on superheater platen wall in CFD model. The exchanged values are temperature (T), from 1D-PM to CFD, and surface heat transfer (q), from CFD to 1D-PM. b) The coupling-decoupling strategy.

Chapter 4

Results and Discussion

In this chapter, the following results are presented and discussed:

- Validation of the developed 1D-PM modelling approach with reference data in Section 4.1.
- Convergence of integrated CFD/1D-PM simulations in Section 4.2.
- The comparison for flue gas side results between standalone CFD simulation and integrated CFD/1D-PM simulations was performed. The analysis showed only minor differences. Therefore, the results are not included here.
- The flue gas side results of integrated CFD/1D-PM simulations including flue gas flow and temperature fields in superheater region, and heat transfer to boiler walls and superheater platens in Section 4.3.
- The steam side results of integrated CFD/1D-PM simulations including platen-wise pressure losses and generated steam properties in Section 4.4.1. The results are also compared with baseline estimation or standalone 1D-PM simulation.
- The comparison among integrated CFD/1D-PM simulations, standalone 1D-PM simulation and measurements for platen-wise material temperature distribution is presented in Section 4.4.2.
- The feasibility and benefits of integrated CFD/1D-PM simulations in Section 4.5.

4.1 Validation of 1D-PM modelling approach

The consistency and accuracy of the developed 1D-PM are analysed by comparing its simulation results with reference data. The main purpose of this validation study is to understand the working behaviour of developed 1D-PM and obtain its numerical solution that corresponds well with reference data with minimum error. The boundary conditions for 1D-PM are based on reference data. The inlet and outlet boundary conditions, and desuperheating water properties are shown in Table 3.7. The thermal

boundary conditions to superheater platens are uniform heat flux distribution, which is a common assumption when no more detailed information is available. The platen-wise heat flux distribution to superheaters is described in Table 4.1.

Table 4.1: Heat flux distribution to supherheaters′ platens based on reference data.

Superheaters	q_{total} [kW]	Platens	q_{platen} [kW]	q''_{platen} [kW/m^2]
SH1A	3814	21	181.62	4.75
SH1B	3566	21	169.81	5.71
SH2	9773	21	465.38	9.89
SH3	8209	21	390.90	7.72
SH4	3017	21	143.67	3.75

The comparison between reference data and simulation results of 1D-PM including inlet and outlet pressures, pressure losses across the superheaters, steam temperatures, and final superheated steam properties are shown in Tables 4.2, 4.3 and 4.4. It can be seen that the computed results of 1D-PM are in good agreement with the reference data. The maximum deviations of 9% and 7% are found for the pressure losses across the SH1B and SH4 respectively. The differences between pressure losses across other superheaters including SH1A, SH2 and SH3 are less than 5%. Similarly, small discrepancies ($\leq$3%) are found between calculated values of steam temperature and respective reference data values.

The steam mass flow rate simulated by 1D-PM is similar to reference data as shown in Table 4.4. It is noted that for the same outlet steam mass flow rate, the outlet steam pressure and temperature are deviated from reference data by 1.4% and 1% respectively. Moreover, it is also observed that the calculated inlet and outlet values including pressure and temperature are different from the reference data. However, the deviations are small and in the range of 0.4%-1%. The main reasons for above mentioned discrepancies and variations in main steam properties are pipe friction and form losses due to the complex geometries of connecting pipes, headers and superheater platens including piping arrangement in flow loops. The calculation procedure of T-junctions, used to model the inlet and outlet headers, could also contribute for these differences. Therefore, based on this validation study, the consistency as well as accuracy of the developed 1D-PM modelling approach is considered good.

Table 4.2: Comparison between reference data and developed 1D-PM for inlet pressure, outlet pressure and pressure losses for superheaters.

	Reference data			1D-PM		
	p_{in} [bar]	p_{out} [bar]	Δp [bar]	p_{in} [bar]	p_{out} [bar]	Δp [bar]
SH1A	121.74	121.33	0.41	121.85	121.42	0.43
SH1B	121.33	120.98	0.35	121.42	121.04	0.38
SH2	120.81	118.61	2.20	120.37	118.09	2.28
SH3	117.53	115.49	2.04	117.20	115.06	2.14
SH4	114.49	111.89	2.60	113.97	111.20	2.77

Table 4.3: Comparison between reference data and developed 1D-PM for inlet temperature, outlet temperature and total superheating for superheaters.

	Reference data			1D-PM		
	T_{in} $[^oC]$	T_{out} $[^oC]$	ΔT $[^oC]$	T_{in} $[^oC]$	T_{out} $[^oC]$	ΔT $[^oC]$
SH1A	327	341	14	325.8	339.5	13.7
SH1B	341	359	18	339.5	357.6	18.1
SH2	357	426	69	354.5	422.6	68.1
SH3	412	485	73	409.5	481.3	71.8
SH4	478	506	28	474.1	501.3	27.2

Table 4.4: Comparison between reference data and developed 1D-PM for main steam properties.

	Reference data	1D-PM	Relative error [%]
p, bar	111.9	110.29	-1.4
T, ^oC	506	501.3	-1.0
$\dot{m}$, kg/s	38.2	38.2	

4.2 Convergence of integrated CFD/1D-PM simulations

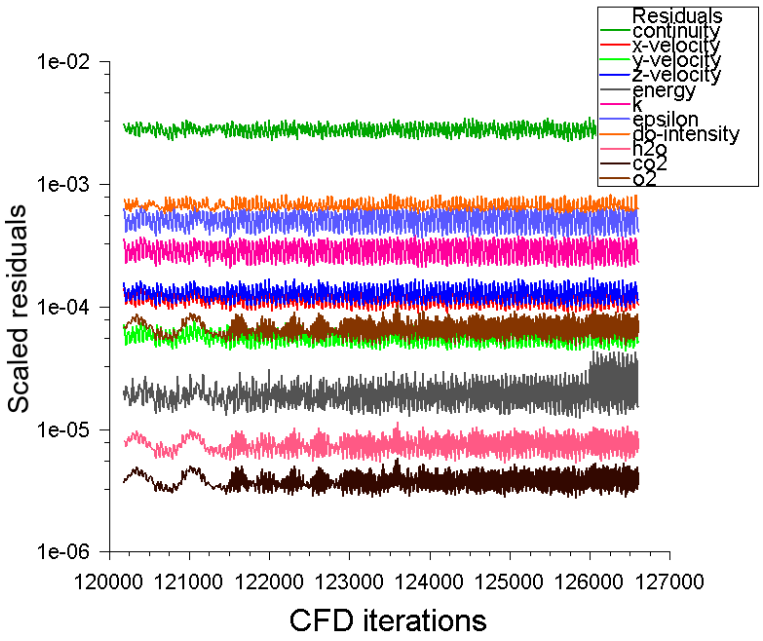

Figure 4.1: The scaled residuals of measured quantities for last 6500 iterations during integrated CFD/1D-PM simulations.

Figure 4.1 shows the scaled residual values of simulated quantities for last 6500 iterations. It can be seen that the residuals do not decrease anymore along the

CFD iterations. However, some fluctuation remains in the residuals, which indicates that iterative convergence is not achieved in a precise way. The researchers such as Maakala et al. [29] and Grace et al. [51] noted that this kind of behaviour is typical in recovery boiler simulations because of their complex geometries and high Reynolds number flue gas flows. In addition to this, the transient behaviour of 1D-PM along with exchanging the boundary conditions including heat transfer rates and temperature at each CFD iteration may also cause the steady state RANS solution to not achieve iterative convergence perfectly.

On the other hand, some results of integrated CFD/1D-PM simulations including total heat transfer rates to SH2 and SH3, and main steam pressure and temperature are shown in Figure 4.2. It is noticed that the solution of heat transfer to SH2 and SH3 during steady state RANS analysis does not change iteration to iteration. Simultaneously, the transient 1D-PM simulation also achieves the steady state as the steam pressure and temperature do not vary along the 1D-PM iterations. Therefore, based on these observations, the solution of integrated CFD/1D-PM simulations is considered converged.

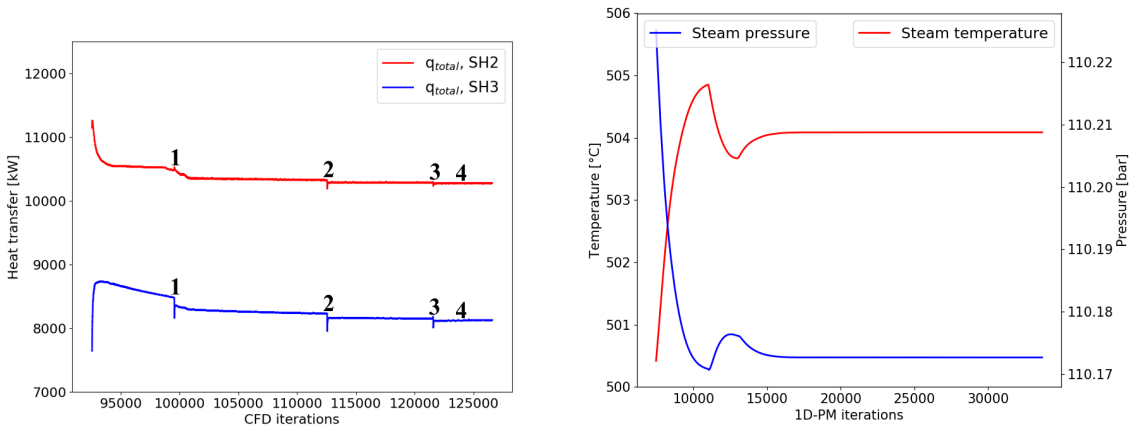

(a) (b)

Figure 4.2: The simulated quantities during integrated CFD/1D-PM simulations. a) The total heat transfer rates to SH2 and SH3. The other superheaters have similar behaviour. 1-4 represent the stages of coupling-decoupling strategy. b) The main steam pressure and temperature.

4.3 Flue gas side results of integrated CFD/1D-PM simulations

The flue gas side results for integrated CFD/1D-PM simulations are discussed in this section. Actually, standalone CFD simulation was also carried out before performing the integrated CFD/1D-PM simulations. In standalone CFD simulation, the convective heat transfer wall boundary conditions including β_{total} and T_{ref} were

utilized for superheater platens. The standalone CFD simulation results were then compared with integrated CFD/1D-PM simulations and only small differences were found. This was expected because in both simulations, the total heat transfer rates to superheaters were same. However, the integrated CFD/1D-PM simulations provides detailed heat flux boundary conditions for superheater platens but it does not effect the overall results of flue gas side. Hence, the standalone CFD simulation results are not reported here.

4.3.1 Flue gas flow and temperature fields

The flue gas flow field between superheater platens at different locations in superheater region are shown in Figures 4.3 and 4.4a. Three recirculation zones are identified and represented by 1, 2 and 3 in the figures. These kind of vortex structures at different locations are also noted in other recovery boiler simulations such as Saviharju et al. [23] and Maakala et al. [28, 29]. The recirculation zones 2 and 3 are located in the corner of front cavity and below the SH4 platens respectively. These vortices are small in size and do not extend along the flue gas flow in the superheater region. It is seen that these small vortex structures do not affect the flue gas temperature field in superheater region significantly.

Moreover, it is observed that the larger recirculation zone (1) is located in the middle of the superheater region that extends from SH2 platens to mainly SH4 platens. There are two main reasons for the occurrence of this large recirculation zone. First, it is mentioned that the recovery boiler is operating at 80% of its total capacity. Therefore, a smaller amount of flue gas enters the superheater region compared to the situation when the recovery boiler operates at its full capacity. Engblom et al. [52] also noted the effect of partial furnace load on asymmetries in flue gas flow field in recovery boiler using both measurements and CFD simulations.

Second, it is seen that the inlet velocity (see Figure 4.3d), taken from previously performed CFD simulation for black liquor combustion in furnace, is not uniform. It is noticed that most of the flue gas flows in the front cavity and above the rear wall. The observations indicate that the non-uniformity of the inlet velocity profile is connected to the non-uniform distribution of the flue gas flow field in superheater region and responsible for the extension of this large recirculation zone (1).

Figure 4.4b shows the flue gas temperature field in the middle of superheater region. It is observed that flue gas flow field substantially affects the flue gas temperature field. The flue gas temperature in large recirculation zone is in the range of 440-530^oC, which is lower than the surrounding flue gas temperature. It is obvious from the observations that the surface areas of superheater platens in this recirculation zone (1) are inefficiently used for heat transfer. Hence, it can be said that the uneven flue gas flow in superheater region leads to non-uniform heat flux distribution to superheater platens, and variation in platen-wise generated steam properties and material temperature distribution in 1D-PM, which are analysed in detail in Sections 4.3.3 and 4.4.

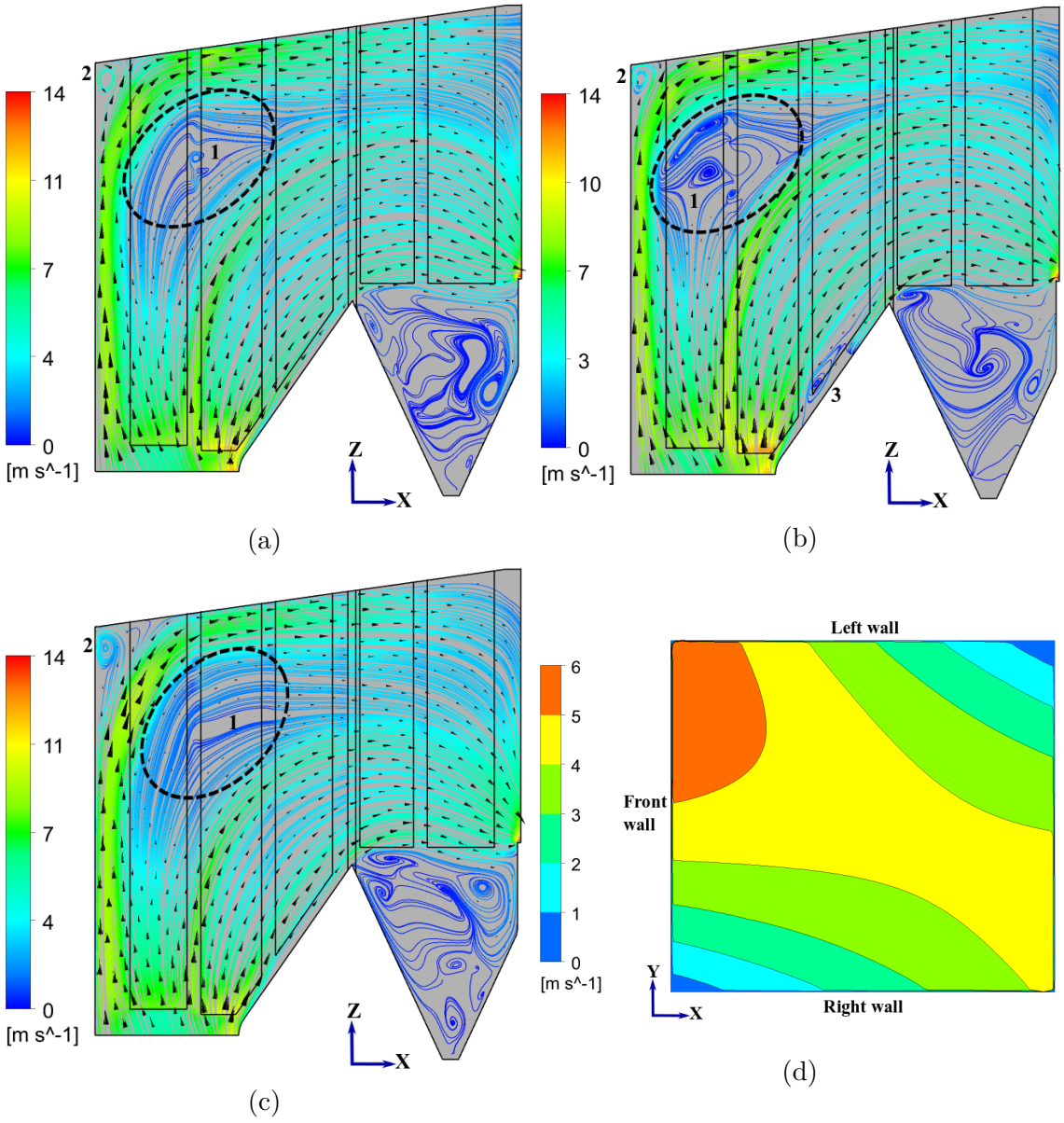

Figure 4.3: The flue gas flow field in superheater region at different distances from right boiler wall in Y-direction and development of recirculation zones. a) At 2.37 m or between platens 7 and 8. b) At 3.61 m or middle of the boiler. c) At 4.86 m or between platens 15 and 16. The locations of recirculation zones are represented by 1, 2 and 3. d) Flue gas velocity (Z-direction) at inlet of current computational domain.

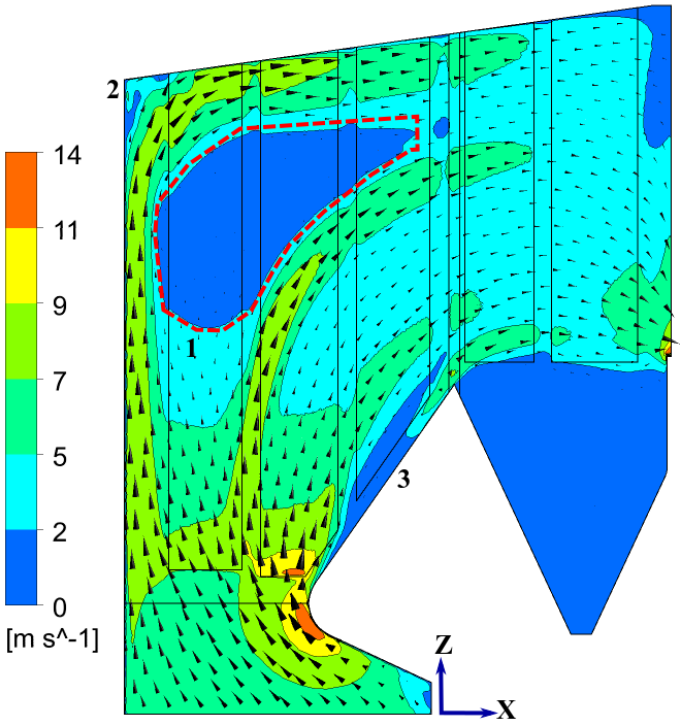

(a)

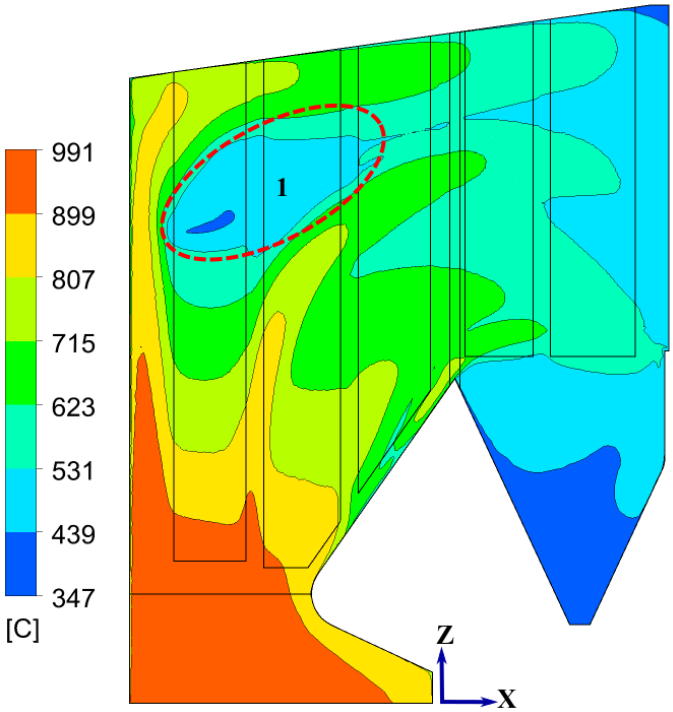

(b)

Figure 4.4: a) The solved velocity field for the flue gas. b) The solved flue gas temperature field. 1, 2 and 3 represent the recirculation zones. These figures are taken from the middle of the boiler width (Y-direction).

4.3.2 Radiation and convection heat transfer

Figure 4.5a shows the total heat flux including radiation and convection to the boiler walls. It is observed that the heat flux to the boiler walls′ surfaces near the inlet is higher. It reduces sharply in the superheater region because the flue gas flows through the passages among the superheater platens and transfers heat to the platens. It is also seen that the 3D flue gas flow field affects the heat flux distribution on the boiler walls. For instance, the heat flux to the middle parts of boiler walls is higher compared to the corners. Moreover, the non-uniformity of the flue gas flow and temperature fields (mostly due to the effect of inlet boundary conditions) can also be seen in the left-right symmetry of the contours in Figure 4.5.

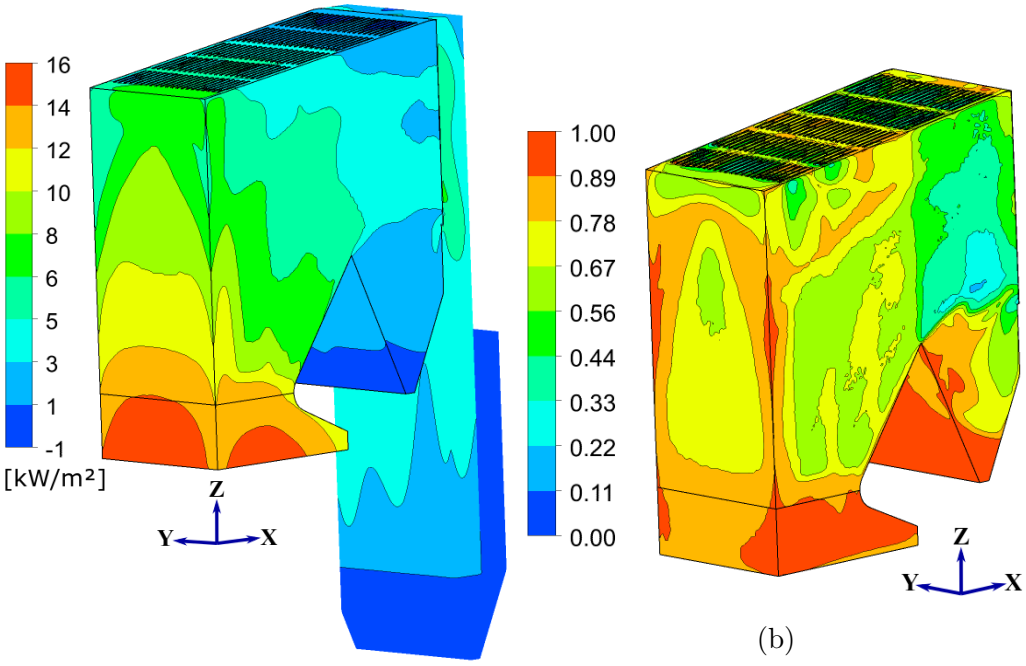

(a) (b)

Figure 4.5: a) The total heat flux to the boiler walls. b) The ratio of radiation heat flux to total heat flux for boiler walls.

It is analysed that approximately 60% of total heat flux on the boiler walls in the simulated region is contributed by radiation. Figure 4.5b shows the ratio of radiation heat flux to total heat flux on the boiler walls. It is clearly visible that the ratio is higher (0.70-1.0) for the surfaces near the inlet and in front cavity. These surfaces are located above the furnace and hence, are exposed to higher radiation. The ratio decreases when the flue gas flows in the superheater region. It means that the relative contribution of convective heat transfer to the boiler walls is increasing along the flue gas flow direction.

The 3D heat flux distribution to the superheaters in the flue gas flow direction is shown in Figure 4.6a. It is observed in Figure 4.6b that the total heat flux to SH2

and SH3 is higher compared to other superheaters including SH4, SH1B and SH1A. The reason is that SH2 and SH3 are exposed to higher flue gas temperature and radiative heat transfer from the flue gas as they are located above the furnace.

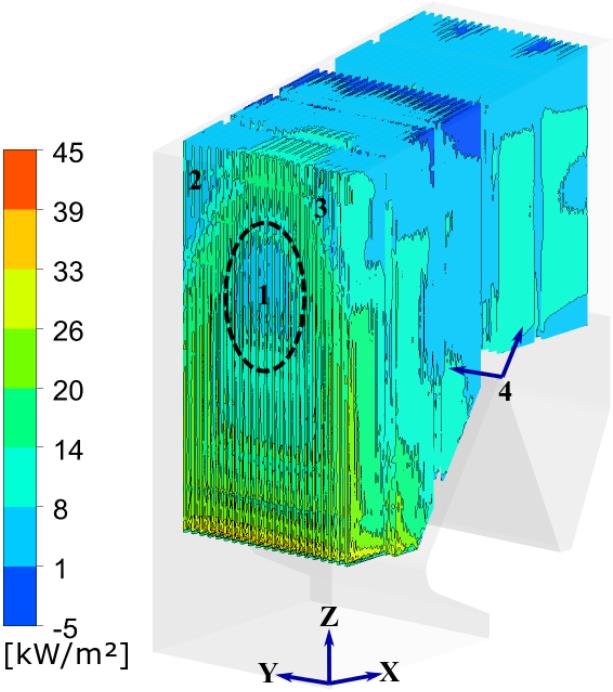

(a)

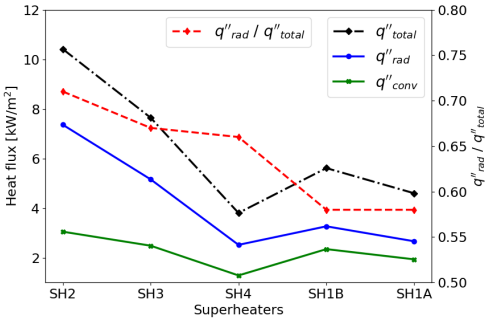

(b)

Figure 4.6: a) The total heat flux to the superheater platens. 1) recirculation zone, 2 and 3) vortex structures in front cavity, and 4) local variation in heat flux distribution to superheater platens. b) The total heat flux, radiation heat flux, convection heat flux and ratio of radiation heat flux to total heat flux for superheaters.

The simulation results indicate that 3D flue gas flow field in superheater region significantly affects the 3D heat flux distribution to the superheater platens as shown in Figure 4.6a. The vortex structures in the corner of front cavity mainly affect the heat flux distribution to the surfaces of SH2 platens near the side walls including left and right walls (regions 2 and 3) as it does not extend along the flue gas flow in superheater region. However, the larger recirculation zone (1) in the middle of the superheater region has substantial effect on heat flux distribution to the superheater platens. For example, the heat flux on the SH2 platens′ surfaces located in this recirculation zone is lower compared to the platens′ surfaces that are outside of this zone. The similar behaviour of non-uniform 3D heat flux distribution is also observed for other superheaters. The flue gas flow field in superheater region is also responsible for local variations (4) in heat flux distribution to superheaters. In addition, it is also noticed that some areas of SH4 platens′ surfaces in large recirculation zone (1) have small amount reverse heat transfer from steam side to flue gas side. In these areas, it is found that the generated steam temperature is little higher than the flue

gas temperature locally. However, in these regions, the flue gas still transfers the heat to boiler walls that are colder than the flue gas.

The results indicate that both convection and radiation substantially contribute for heat transfer to superheater platens as shown in Figure 4.6b. It is noticed that the convective heat flux to superheater platens is clearly more uniform compared to radiative heat flux. The analysis reveals that the ratio of radiation heat flux to total heat flux is higher for SH2 (0.71), SH3 (0.67) and SH4 (0.66). The reason is that along with their locations in the superheater region, the flue gas velocity in the larger recirculation zone is very low. Therefore, most of the heat flux to the superheater platens in this recirculation zone as well as their lower parts is transferred mainly by thermal radiation.

4.3.3 Heat flux distribution to superheater platens

The heat flux distribution on superheater platens for integrated CFD/1D-PM simulations is shown in Figure 4.7. In the figure, the platen-wise heat flux distribution for standalone 1D-PM simulation is also shown for reference. For standalone 1D-PM simulation, the total heat flux to an individual superheater is obtained from integrated CFD/1D-PM simulations and distributed as uniform boundary conditions among the platens. This uniform platen-wise heat flux distribution is then utilized for the comparison study in Section 4.4.

It is visible that the flue gas flow field in superheater region substantially affects the heat flux distribution on the superheater platens. It is observed that the large recirculation zone in the superheater region leads to lower heat flux on the middle SH2 platens compared to platens near side walls as seen in Figure 4.7a. The similar behaviour of non-uniform heat flux distribution to other superheater platens including SH3, SH4, SH1B and SH1A can also be seen in Figures 4.7b, 4.7c, 4.7d and 4.7e respectively. The largest differences for platen-wise heat flux distribution are noted for SH4 and SH1A, where the heat fluxes on the platens near the side walls are respectively 83% and 80% higher than the platens in the middle region.

In addition, for SH3, SH4, SH1B and SH1A, it is seen that the heat fluxes on their middle platens (8-12) are higher compared to their neighbouring platens. This W-shaped heat flux distribution is caused due to the size and shape of the large and cold recirculation zone. It is noticed during the analysis that the recirculation zone after SH2 platens starts to separate towards the side walls. Therefore, the total heat flux including radiation and convection on the middle platens of these superheaters starts to increase and hence, is higher than their neighbouring platens.

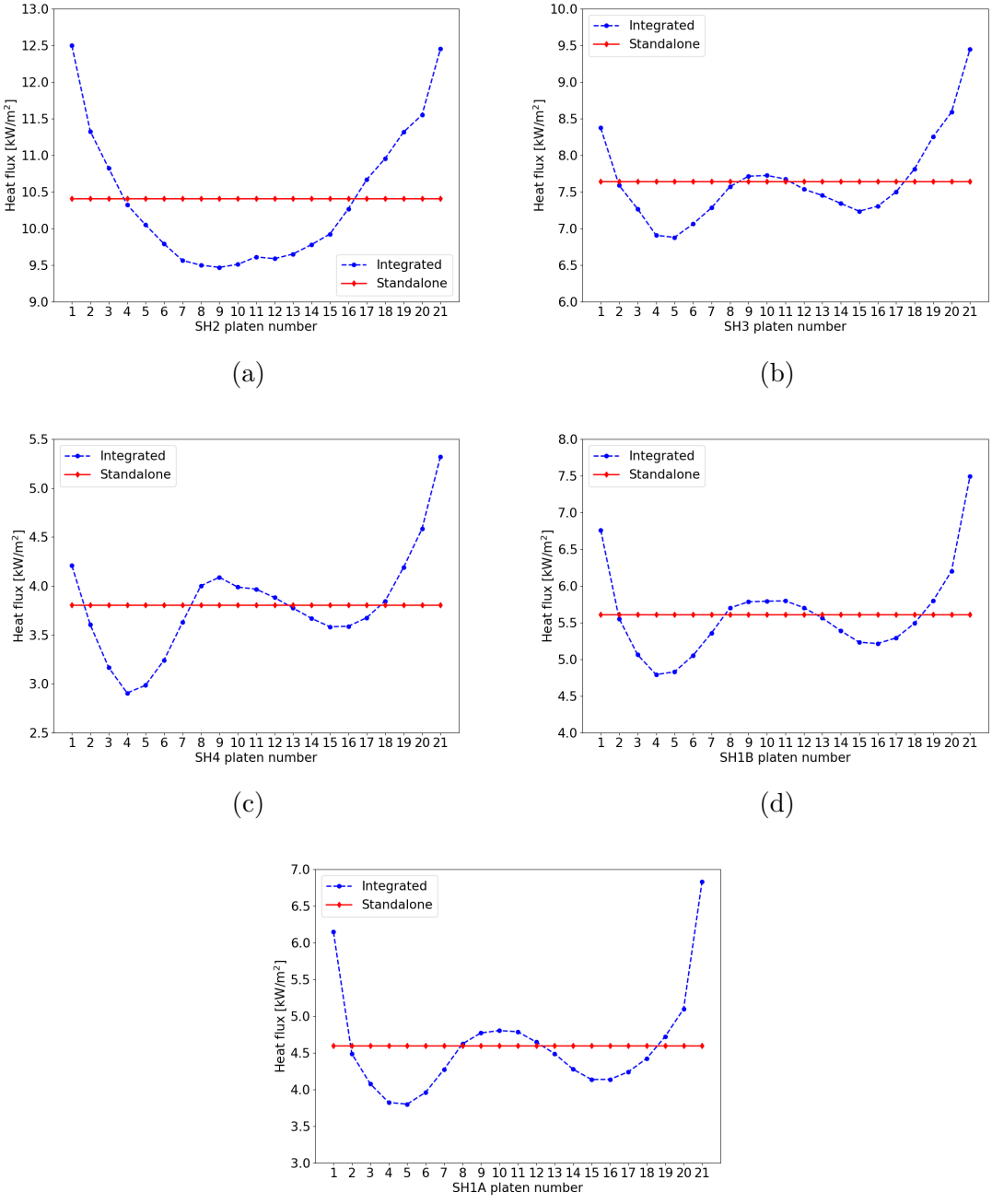

Figure 4.7: Heat flux distribution to superheater platens for integrated CFD/1D-PM simulations along the flue gas flow in superheater region. The total heat flux to a superheater is taken from integrated CFD/1D-PM simulations and then distributed as uniform boundary conditions among its platens for standalone 1D-PM simulation. It is done to carry out comparison study between integrated CFD/1D-PM and standalone 1D-PM simulations in Section 4.4.

4.4 Steam side results of integrated CFD/1D-PM simulations

The steam side results for integrated CFD/1D-PM simulations and their comparison with standalone 1D-PM simulation results are presented and discussed in this section. The comparison study is performed to analyse the effect of non-uniform heat flux distribution on platen-wise generated superheated steam properties and material temperature distribution compared to commonly assumed and used uniform heat flux distribution approach for superheated steam generation cycle. Eventually, the analysis results will explicitly show the effect of the integration modelling approach on the steam side results.

The final superheated steam properties calculated during integrated CFD/1D-PM simulations and standalone 1D-PM simulation are very close to each other (see Table 4.5). Moreover, the total outlet steam mass flow rate from each superheater is shown in Figure 4.8. For both simulation approaches, it is noticed that the geometrical structure of main steam pipe plus associated friction and form losses cause variation in outlet steam mass flow rates for SH4 outlet header.

4.4.1 Platen-wise pressure losses, mass flow rates and temperature

The platen-wise distribution of inlet and outlet superheated steam pressures, pressure losses, mass flow rates and steam temperature for superheaters SH1A, SH1B, SH2, SH3 and SH4 are shown in Figures 4.9, 4.10, 4.11, 4.12 and 4.13. The results for superheaters are presented in the order of superheating stages (1-4) of steam cycle as shown in Figure 3.6.

Pressure losses

For SH1A platens, the simulated values for pressure losses during integrated CFD/1D-PM and standalone 1D-PM simulations are very similar to each other as shown in Figure 4.9c. The maximum difference of 2.4% is found for platens 1 and 21. It is noticed that the sharp change in platen-wise pressure losses are also caused by four cross-junctions in SH1A inlet header, where the pipes from steam drum are connected. These cross-junctions are represented as 1, 2, 3 and 4 in Figure 4.9a. In addition to this, it is mentioned earlier that SH1A platens are directly connected to individual SH1B platens. Therefore, the variation in pressure losses for SH1B platens (see Figure 4.10c) in integrated CFD/1D-PM and standlaone 1D-PM simulations behave similarly to pressure losses among SH1A platens. However, the maximum deviation of 6% between integrated CFD/1D-PM simulations and standalone 1D-PM simulation results is obtained for SH1B.

For SH2, SH3 and SH4, the platen-wise pressure losses calculated during integrated CFD/1D-PM simulations are higher than the standalone 1D-PM simulation as shown in Figures 4.11c, 4.12c, 4.13c. For both integrated CFD/1D-PM and standalone

1D-PM simulations, the differences in pressure losses are low and in range of 1.86%, 1.5% and 0.8% for SH2, SH3 and SH4 respectively. In context of SH2 and SH3 platens, the platens near the side walls have higher pressure losses and they decrease in a symmetric way when the steam enters or leaves the platens located in the middle region.

The sharp increment in the pressure losses for middle platen 11 is observed for SH2, SH3 and SH4. At this location, colliding flow in inlet header and diverging flow in outlet header cause sharp variations in velocity head and head losses. Hence, they increase the pressure losses for this platen. Moreover, it is noticed for SH4 that the pressure losses are higher for the platens near the right wall than the platens towards left boiler wall. The main reasons for this discrepancy are the geometrical structure of main steam pipe and associated friction losses and minor losses due to connecting 90° bends. These results indicate that the pressure losses computed during integrated CFD/1D-PM simulations and standalone 1D-PM simulation are close to each other with small discrepancies.

Steam mass flow rate distribution

The platen-wise mass flow rates for SH1A, SH1B, SH2, SH3 and SH4 are shown in Figures 4.9d, 4.10d, 4.11d, 4.12d and 4.9d. For both integrated CFD/1D-PM and standalone 1D-PM simulations, the variations in platen-wise steam distribution are caused by variations in pressure losses or in static pressure differences along the superheater platens, and heat flux distribution.

The comparison study between integrated CFD/1D-PM and standalone 1D-PM simulations shows that the maximum difference between platen-wise steam distribution for SH1A and SH1B is 2.3% whereas it is 2.2%, 1.09% and 0.56% for SH2, SH3 and SH4 platens respectively. In context of platen-wise steam distribution during integrated CFD/1D-PM simulations, the deviations between maximum and minimum mass flow rates are largest (7%) for SH1A and SH1B platens whereas for other superheater platens, the differences are below 3%. Therefore, based on these observations, it can be said that the 3D heat flux distribution in superheater region has smaller impact on platen-wise steam mass flow rate distribution compared to the pressure losses due to complex geometries of headers, connecting pipes and superheater platens including the structures of flow loops.

Steam temperature distribution

The platen-wise inlet and outlet steam temperatures for SH1A, SH1B, SH2, SH3 and SH4 for both integrated CFD/1D-PM and standalone 1D-PM simulations are shown in Figures 4.9e, 4.10e, 4.11e, 4.12e and 4.13e. The platen-wise superheating of the steam is shown in Figures 4.9f, 4.10f, 4.11f, 4.12f and 4.13f. It is clearly visible that the 3D-flue gas flow field in superheater region substantially affects the platen-wise generated superheated steam temperatures as it is responsible for non-uniform heat flux distribution on superheater platens.

The platens near side walls as well as platens (8-12) located in middle region in case of SH3, SH4, SH1B and SH1A have higher steam temperatures. The reason is that these platens have higher heat fluxes compared to other platens for an individual superheater. On the other hand, the standalone 1D-PM simulation that is based on commonly assumed uniform heat flux distribution approach provides almost similar platen-wise steam temperatures for the superheaters. Therefore, the superheated steam generation process based on uniform heat flux approach is not accurate as it does not consider the effect of flue gas flow field in superheater region.

In context of integrated CFD/1D-PM simulations′ results, the maximum deviations for platen-wise steam superheating are found for SH1A (122%), SH1B (111%) and SH4 (93%) whereas they are approximately 45% for SH2 and SH3. It is also observed that the inlet headers distribute the steam to superheater platens with almost uniform temperature, which indicates their mixing effect. However, for SH1B, the platen-wise inlet temperatures vary significantly as the SH1B platens are directly connected to SH1A platens without the headers. Similarly, small discrepancies in inlet temperatures for SH4 platens are found. These are due to the variations in steam superheating in SH3 platens. Moreover, it is seen in the following Section 4.4.2 that the variation in steam temperature distribution can have a significant effect on the superheater material temperature distribution.

Table 4.5: Comparison between integrated CFD/1D-PM simulations and standalone 1D-PM simulation for main steam properties.

	Integrated CFD/1D-PM	Standalone 1D-PM
p, bar	110.17	110.24
T, ^oC	504	504.1
$\dot{m}$, kg/s	38.2	38.2

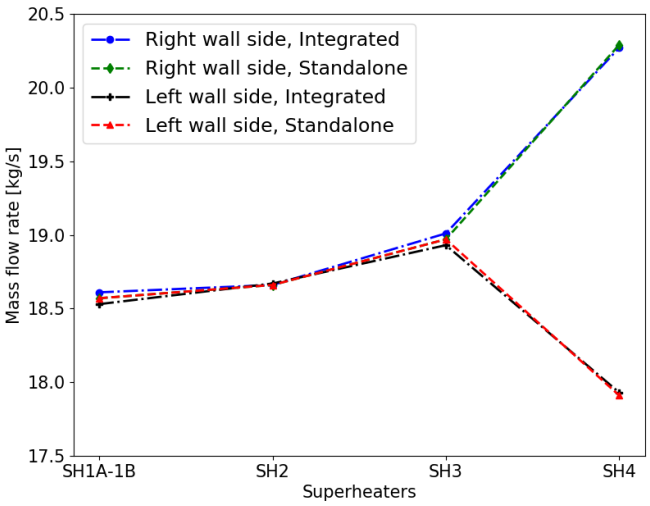

Figure 4.8: The outlet steam mass flow rates from the exits including left wall side and right wall side of outlet headers for all the superheaters.

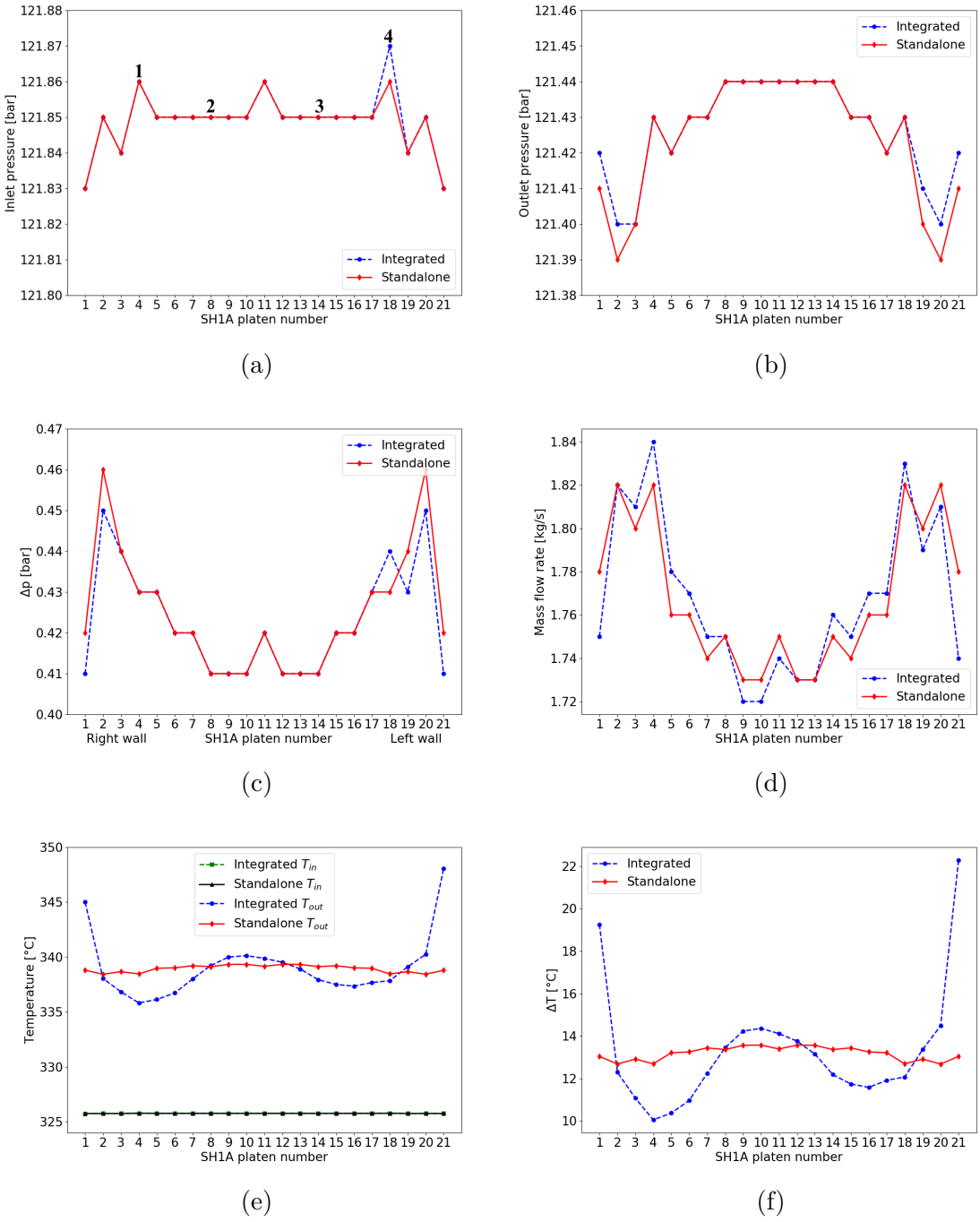

Figure 4.9: SH1A platen-wise a) inlet pressure, b) outlet pressure, c) pressure losses, d) mass flow rates, e) steam temperature and f) total superheating. 1, 2, 3 and 4 in Figure 4.9a represent the connecting pipes from steam drum.

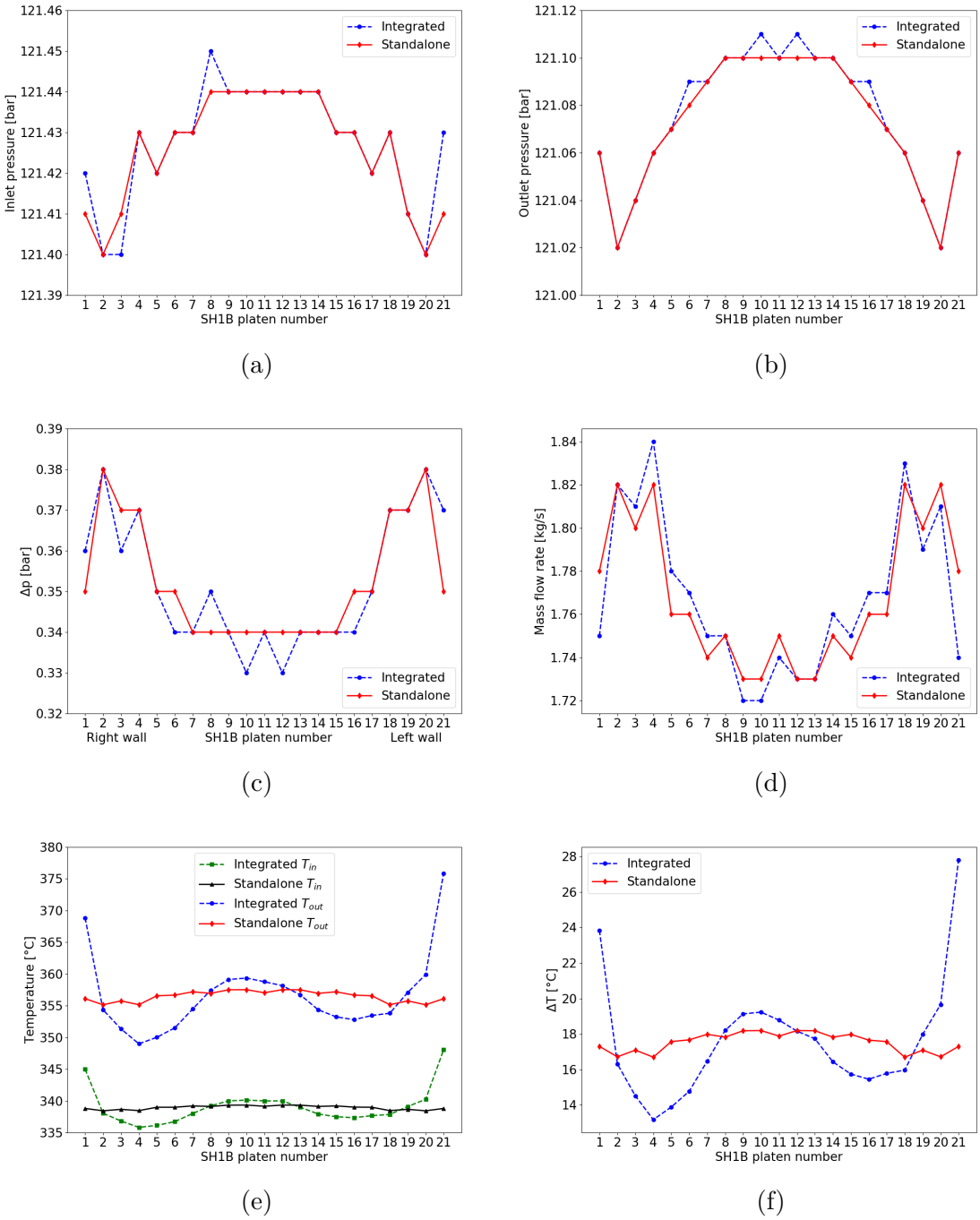

Figure 4.10: SH1B platen-wise a) inlet pressure, b) outlet pressure, c) pressure losses, d) mass flow rates, e) steam temperature and f) total superheating.

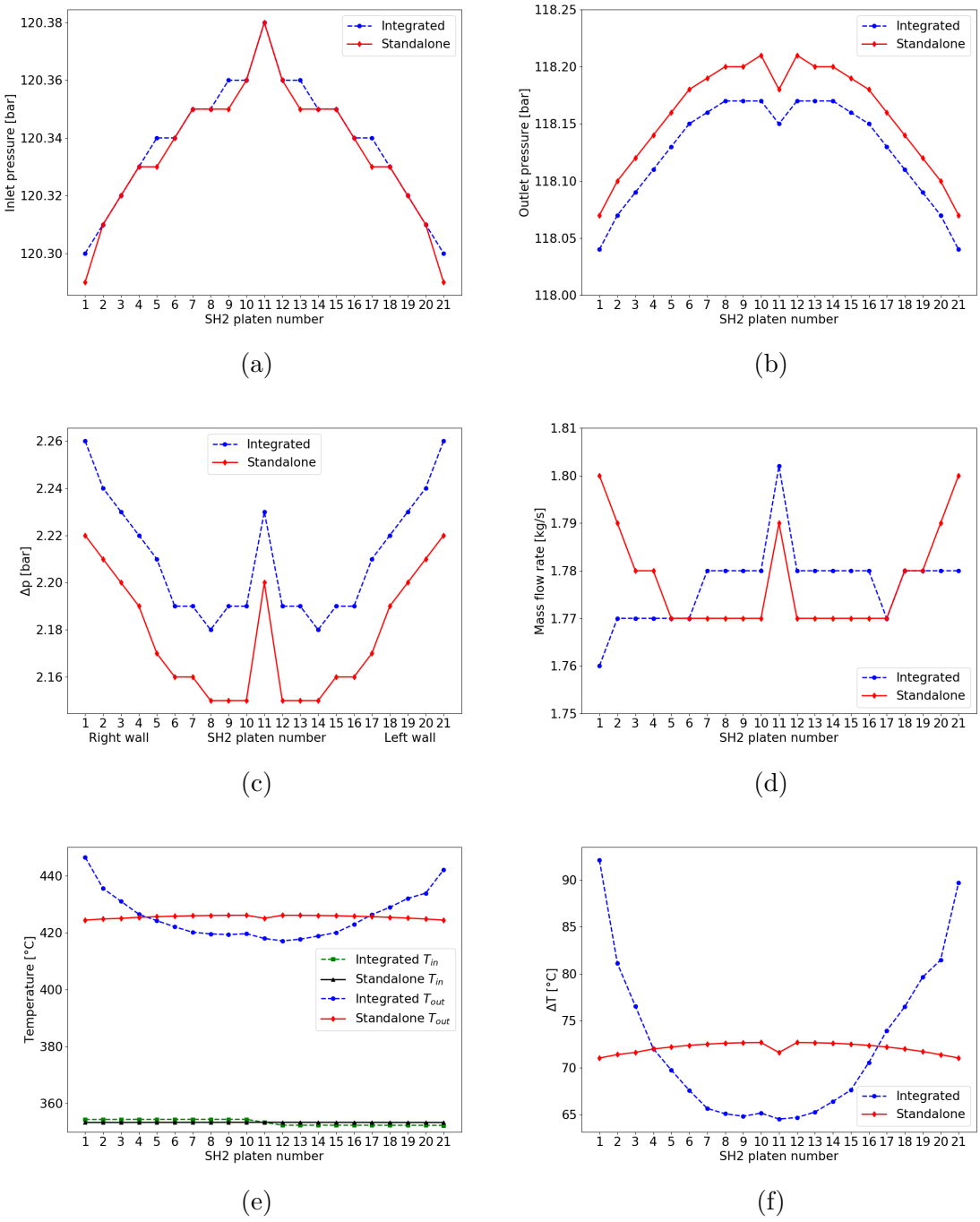

Figure 4.11: SH2 platen-wise a) inlet pressure, b) outlet pressure, c) pressure losses, d) mass flow rates, e) steam temperature and f) total superheating.

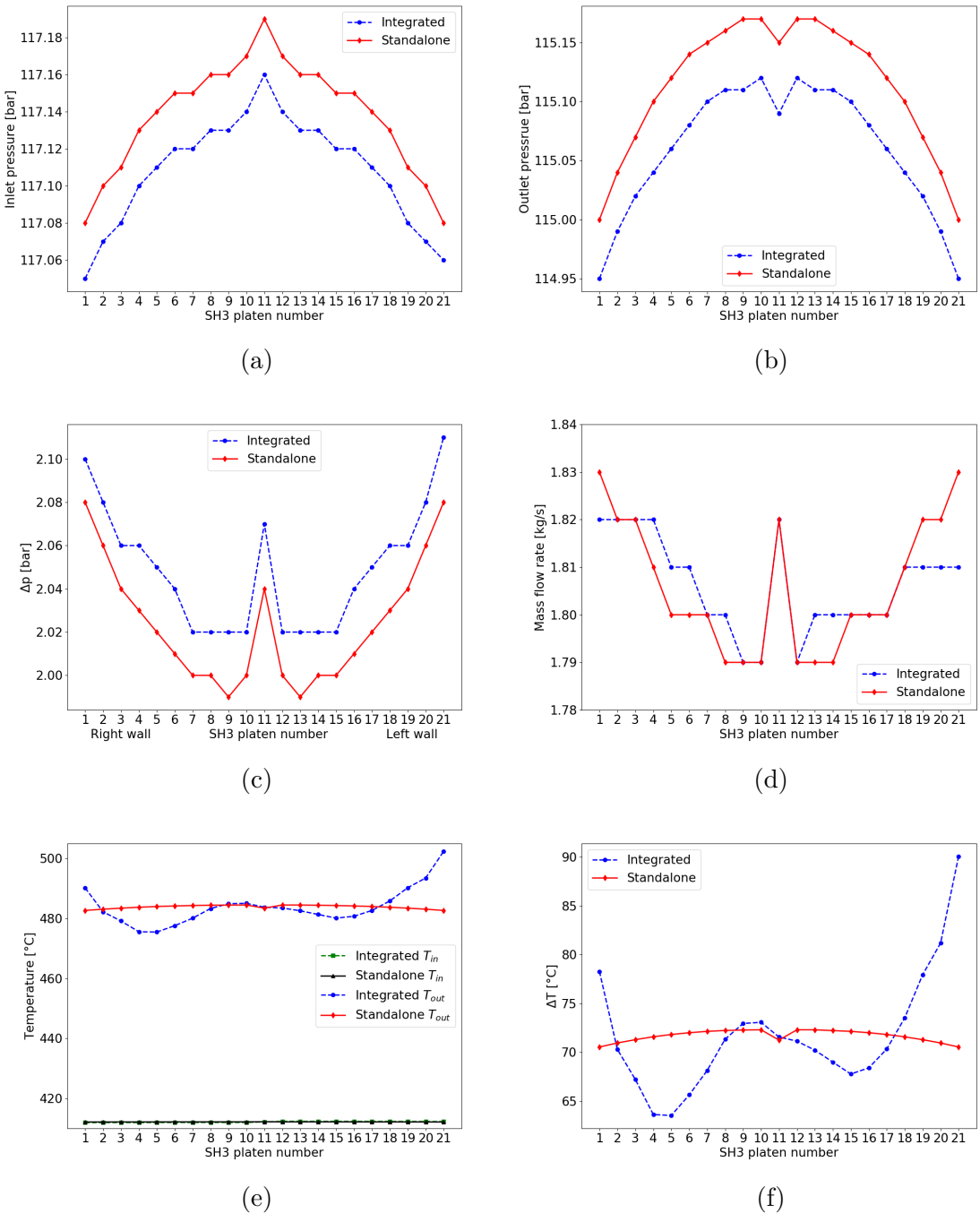

Figure 4.12: SH3 platen-wise a) inlet pressure, b) outlet pressure, c) pressure losses, d) mass flow rates, e) steam temperature and f) total superheating.

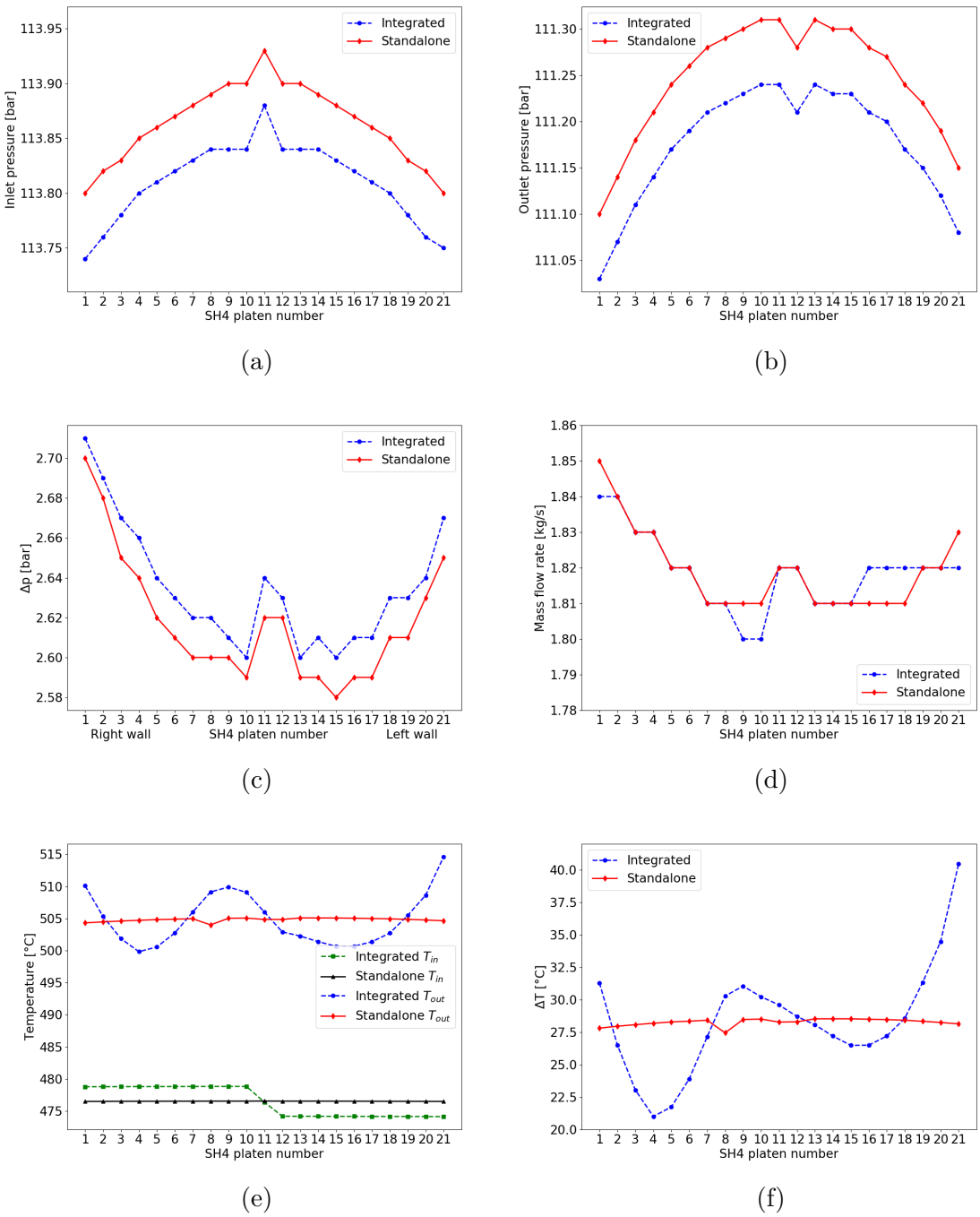

Figure 4.13: SH4 platen-wise a) inlet pressure, b) outlet pressure, c) pressure losses, d) mass flow rates, e) steam temperature and f) total superheating.

4.4.2 Superheater material temperature distribution

Table 4.6 shows typically utilized maximum temperature limits for the superheater materials in recovery boilers. The superheaters should be operated below these temperature limits for safe and efficient recovery boiler operation.

Table 4.6: Maximum superheater material temperature limits according to Standard EN 10216-2 [53].

Superheaters	Material temperature $[^oC]$
SH1A and SH1B	550
SH2 and SH3	600
SH4	670

The thermocouples were installed to measure the superheater material temperatures during the measurement campaign. The locations of these thermocouples are shown in Figure 4.14. For SH1A, SH1B, SH2 and SH4, the material temperatures were measured for each steam flow loop in certain number of platens. However, the material temperatures were not measured for flow loop 2 in selected SH3 platens. Therefore, there are 93 thermocouple measurements available in total. The superheater material temperature during integrated CFD/1D-PM simulations and standalone 1D-PM simulation are taken from similar locations, where the thermocouples are located. The detailed information of the flow loops and their lengths in each superheater platen for the chosen recovery boiler is shown in Table 4.7.

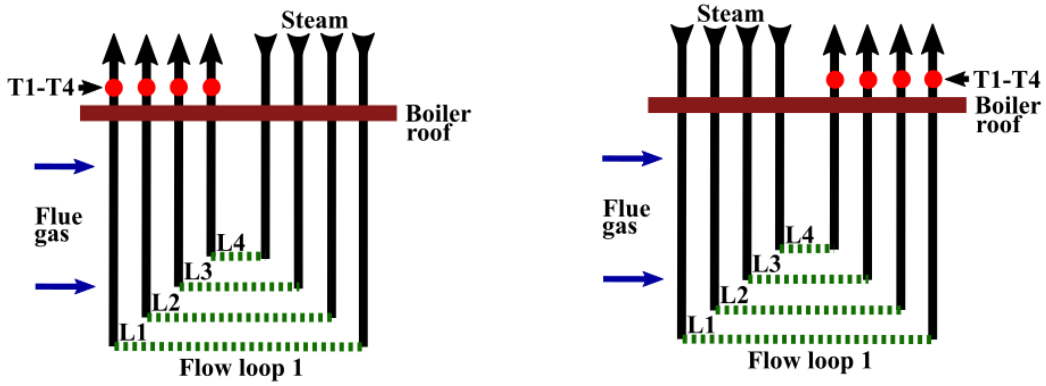

Figure 4.14: The schematic of flow loops in superheater platens. a) SH1A and SH1B. b) SH2, SH3 and SH4. The outermost superheated steam loop is marked as Flow loop 1. L1-L4 represent the lengths of flow loops. In both figures, the dashed lines represent variation in flow loops′ lengths. T1-T4 are the thermocouples for material temperature measurement and they are located above the recovery boiler roof. However, the thermocouples were not installed for flow loop 2 in SH3 platens.

Table 4.7: Number and lengths of superheated steam flow loops in superheaters' platens.

Superheaters	Flow loops	Lengths
SH1A	4	L1 $\approx$ L2 $\approx$ L3 $\approx$ L4
SH1B	4	L1 $\approx$ L2 $\approx$ L3 $\approx$ L4
SH2	3	L1 $<$ L2 $\approx$ L3
SH3	4	L1 $\approx$ L2 $<$ L3 $\approx$ L4
SH4	3	L1 $<$ L2 $\approx$ L3

The comparison among measurements, integrated CFD/1D-PM simulations and standalone 1D-PM simulation is shown in Figures 4.15, 4.16, 4.17, 4.18 and 4.19. It is observed that the simulated values of loop-wise material temperature during integrated CFD/1D-PM simulations and standalone 1D-PM simulation are below the maximum material temperature limits shown in Table 4.6.

In standalone 1D-PM simulation, the heat flux is uniformly distributed among the platens of an individual superheater and hence, each flow loop in a platen receives constant heat flux. The flow loops have similar lengths in SH1A and SH1B platens. Therefore, the calculated material temperatures for all the loops are almost same due to similar amount of heat to the flow loops.

Moreover, in SH2, SH3 and SH4 platens, the flow loops have different lengths. When constant heat flux is applied, the shorter loops receive a smaller amount of heat. Moreover, within one platen, the pressure loss between outlet header and inlet header is same for both shorter and longer loops. However, shorter loops have lower friction and form losses. Hence, they have higher steam mass flow rates compared to the longer flow loops. Therefore, lower superheater material temperatures are observed for shorter loops. For instance, in SH3 platens, outermost loop (Flow loop 1) or L1, and L2 are shorter than L3 and L4. Hence, calculated material temperatures for flow loop 1 and flow loop 2 are lower than flow loop 3 and flow loop 4 as shown in Figure 4.18.

In real recovery boiler operation, the situations are different than standalone 1D-PM simulation. The flue gas flow field in superheater region and generated superheated steam properties cause variations in both platen-wise and loop-wise heat flux distributions. In fact, the integrated CFD/1D-PM simulations are able to capture these detailed phenomena in superheater region. The non-uniform platen-wise and loop-wise heat flux distributions are connected to variations in superheater material temperatures along different platens and their flow loops, which are shown in the figures.

It is mentioned above that in standalone 1D-PM simulation, the calculated material temperature for outermost loop or shorter loop is lower than inner loops or longer loops of a platen due to less heat flow and higher steam mass flow rate. However, in reality, the outermost loop faces directly the flue gas. Therefore, the heat flux to outermost loop is larger compared to other loops of a platen. It is responsible for

higher material temperature for outermost loop even though it is short in length. For example, the material temperatures for outermost loops in SH1A and SH1B platens are higher than the inner loops in both measurement and calculated values of integrated CFD/1D-PM simulations.

Moreover, it is also noticed in case of SH2, SH3 and SH4 platens that even though the inner loops have lower heat flux compared to outermost loops, their total heat transfer rates are higher due to the larger lengths and steam flow areas. Therefore, the material temperatures of outermost loops and inner loops for SH2, SH3 and SH4 platens are close to each other, which can be seen from measured values and the results of integrated CFD/1D-PM simulations.

The effect of variation in flue gas flow fields during measurement campaign and integrated CFD/1D-PM simulations on material temperature distribution can be easily seen in the figures as the loop-wise temperature distribution profiles are little different from each other. However, at some locations, the integrated CFD/1D-PM simulations and measured values show some agreement in material temperature distribution along the platens. For example, the material temperature distribution in flow loops 3 and 4 for SH3 platens (see Figure 4.18). Moreover, Tables 4.8 and 4.9 show the maximum deviations and average differences in material temperatures for superheaters respectively.

Table 4.8: Maximum difference between measured values and results of integrated CFD/1D-PM simulations for superheater material temperature distribution.

Superheaters	Platen number	Flow loop number	Maximum error [%]
SH1A	7	3	1.6
SH1B	7	1	2.5
SH2	5	3	3.2
SH3	10	3	5.7
SH4	10	3	5.0

Table 4.9: Average difference between measurements and integrated CFD/1D-PM simulations for superheater material temperature distribution.

Superheaters	Average difference [%]
SH1A	0.7
SH1B	1.0
SH2	1.5
SH3	2.2
SH4	2.6

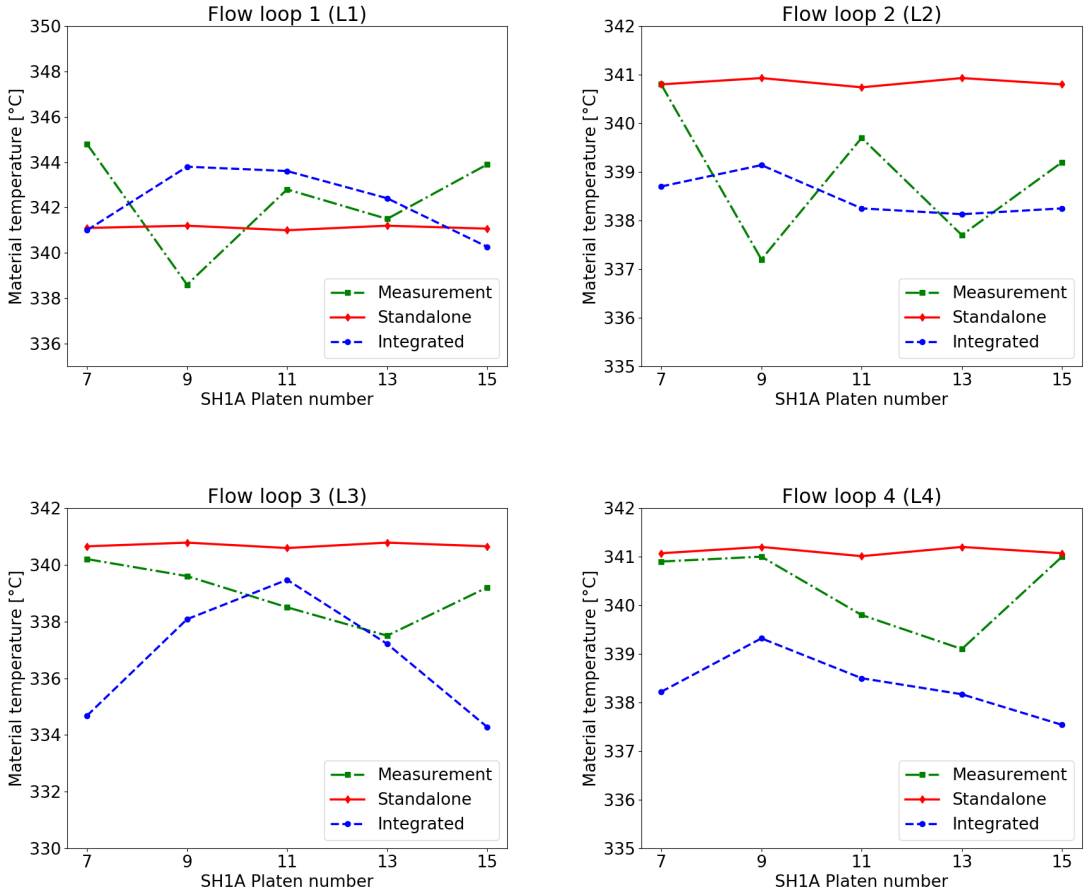

Figure 4.15: Material temperature comparison for SH1A a) Flow loop 1, b) Flow loop 2, c) Flow loop 3 and d) Flow loop 4.

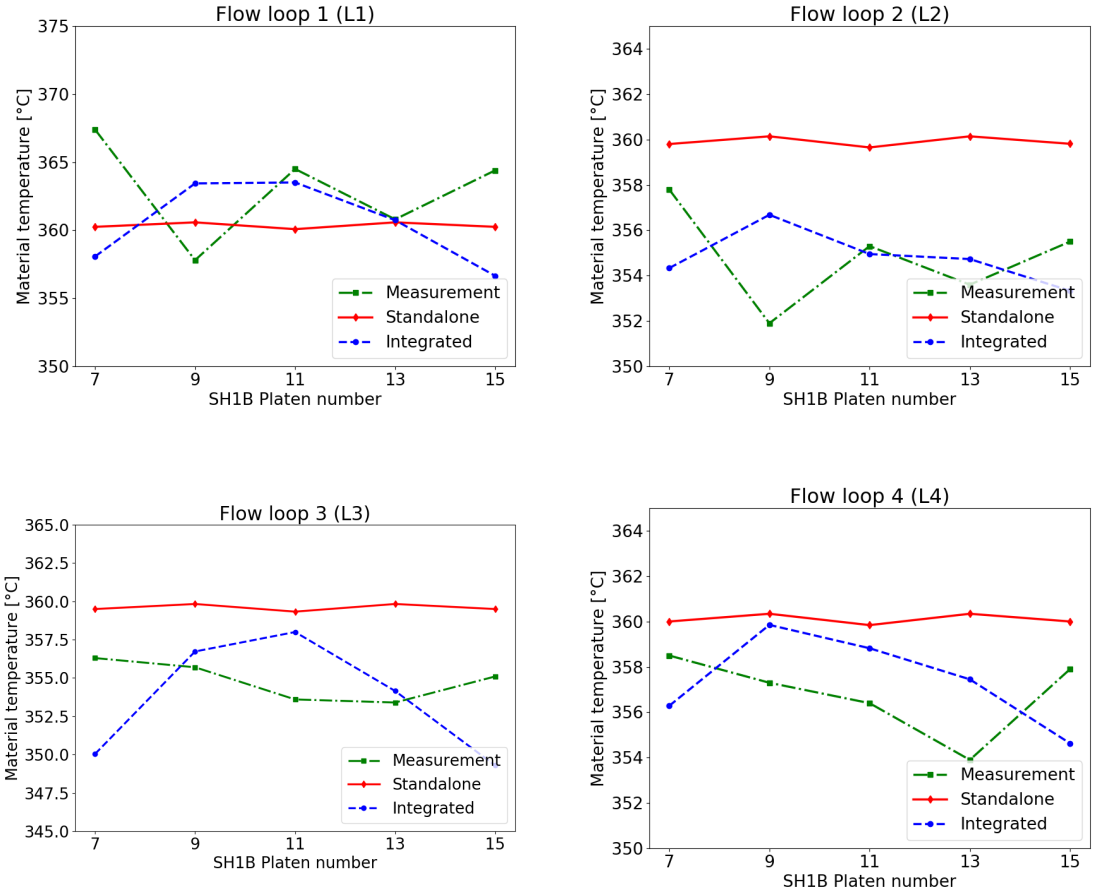

Figure 4.16: Material temperature comparison for SH1B a) Flow loop 1, b) Flow loop 2, c) Flow loop 3 and d) Flow loop 4.

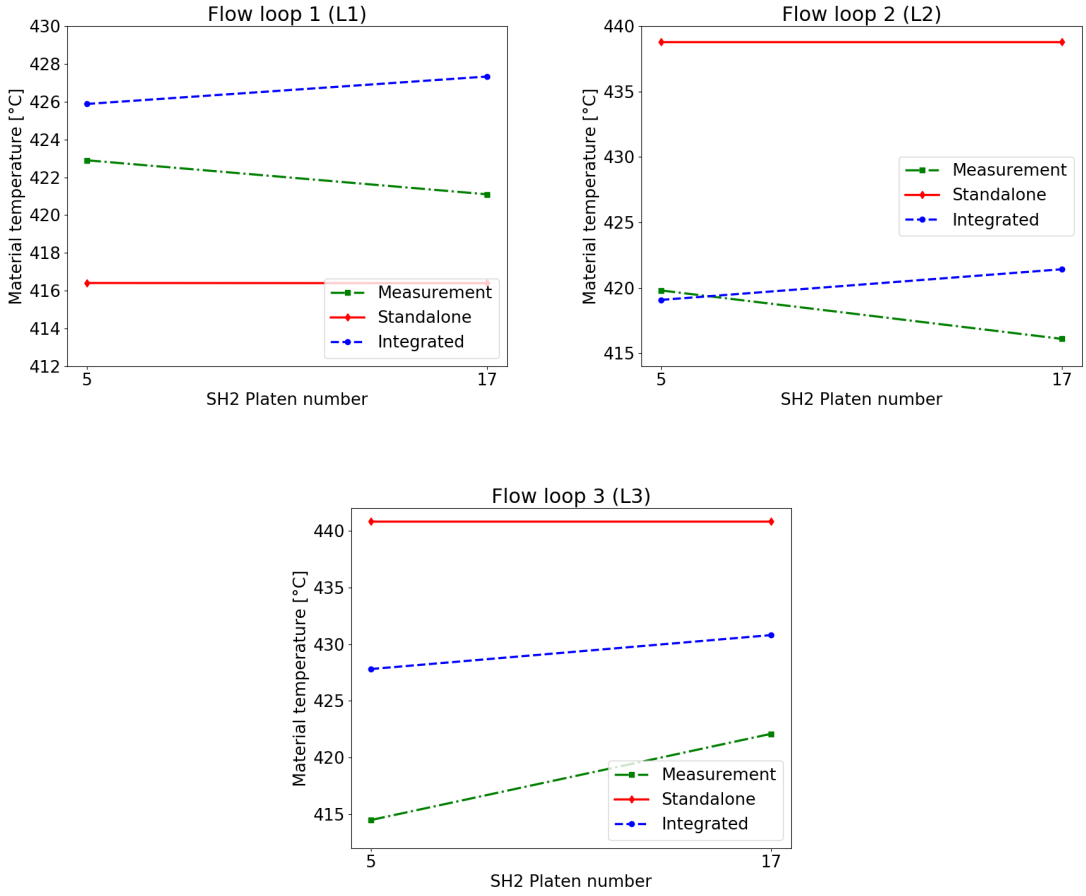

Figure 4.17: Material temperature comparison for SH2 a) Flow loop 1, b) Flow loop 2 and c) Flow loop 3.

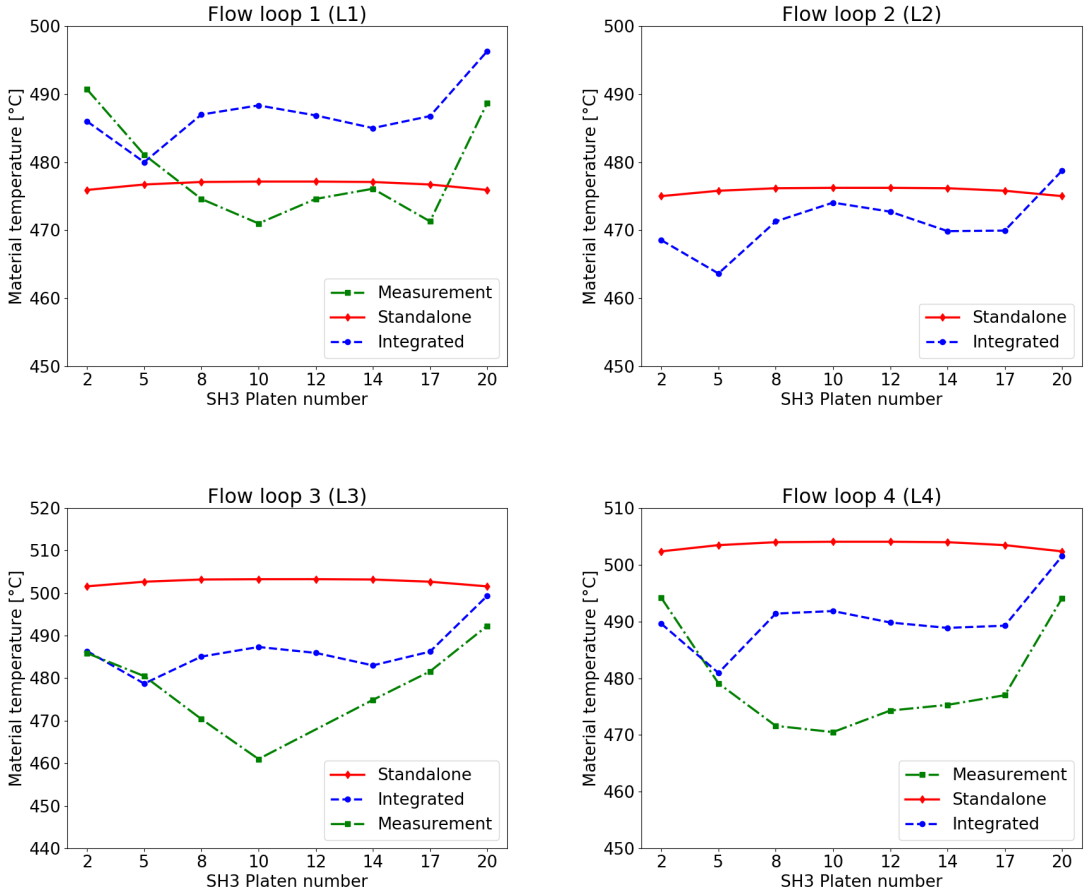

Figure 4.18: Material temperature comparison for SH3 a) Flow loop 1, b) Flow loop 2, c) Flow loop 3 and d) Flow loop 4. The measurement data for flow loop 2 is not available. For platen number 12, the measured value for flow loop 3 is discarded due to the faulty thermocouple.

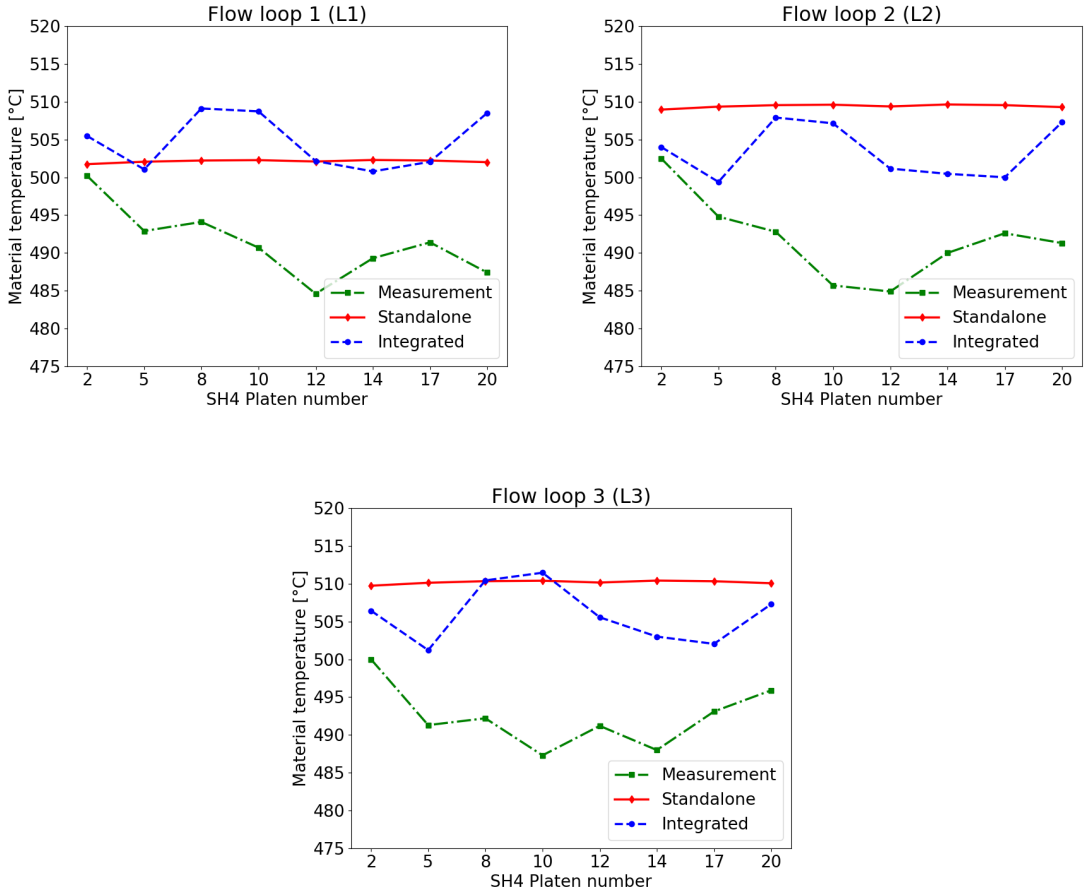

Figure 4.19: Material temperature comparison for SH4 a) Flow loop 1, b) Flow loop 2 and c) Flow loop 3.

4.5 Feasibility and advantages of integrated modelling approach

The analysis reveals that the parameters including heat load and black liquor combustion process in the recovery boiler are connected to flue gas flow behaviour. The unevenness in these parameters is responsible for variations in flue gas flow field and heat flux distribution in the superheater region. The non-uniform heat flux distribution to superheater platens plus complex geometry of steam cycle significantly affect the platen-wise generated steam properties especially temperature, and material temperature distribution. This novel integrated CFD/1D-PM modelling approach is capable to provide the detailed knowledge about these complex phenomena to precisely understand the real recovery boiler operation. These phenomena can not be solved accurately with uniform heat flux distribution approach, which is commonly used for superheated steam generation process.

Furthermore, the feasibility of this integrated CFD/1D-PM modelling approach also depends on various other obvious factors. These important factors are accurate generation of both computational models, discretization of CFD model and 1D-PM, set-up for coupled simulations, computational time and accuracy. In both CFD and 1D-PM models, the precise selections for cell sizing and calculation nodes are very crucial for discretizing the superheater platens and steam flow loops properly. The accurate discretization is important for connecting both computational models and performing integrated CFD/1D-PM simulations proficiently. In addition to this, these complex and detailed integrated CFD/1D-PM simulations require larger computational time and efficient computational resources to achieve the converged solution for both flue gas side and superheated steam cycle.

Therefore, based on these considerations, the developed integration modelling approach is beneficial to investigate the local phenomena for both trouble shooting and optimizing the performance of superheaters. Moreover, in initial stage, the recovery boiler is designed based on average temperature estimation. The integrated CFD/1D-PM simulations are able to precisely provide the information about the accuracy of these estimations for optimizing the design margins in the future. Hence, the integrated CFD/1D-PM simulations are useful for improving the thermal efficiency, cost efficiency and safety of recovery boiler and its superheater region.

Chapter 5

Conclusions

5.1 Summary

In this work, a novel integrated CFD/1D-PM modelling approach was developed for superheater region in the recovery boiler using ANSYS Fluent 18.1 and Apros 6. The aim of this study was to obtain the detailed solution about steam generation process and material temperature distribution for the superheaters. For this purpose, a full scale 3D-CFD model for superheater region was developed and coupled with comprehensive 1D-PM for superheated steam generation cycle.

In the 3D-CFD model, the superheater platens were modelled as flat plates to reduce the complexity and calculation time for the simulation. In the 1D-PM, each flow loop of a superheater platen, headers and main steam pipe were modelled using heat pipe, point and T-Junction components of Apros 6. The two-way heat transfer coupling method was utilized to perform the integrated CFD/1D-PM simulations. The boundary conditions including surface temperature and heat transfer rate were exchanged at every CFD iteration.

Before performing integrated CFD/1D-PM simulations, the developed 1D-PM model was validated using reference data. The uniform heat flux distribution boundary conditions based on reference data were applied to superheater platens. It was found that the geometries of superheater platens, connecting pipes, headers and main steam pipe plus their associated friction and form losses were responsible for platen-wise variations in both pressure losses and steam distribution. However, for an individual superheater, the platen-wise calculated steam temperature values were almost uniform. The calculated main steam pressure and temperature were underestimated by 1.4% and 1.0% respectively.

The integrated CFD/1D-PM simulations revealed that the flue gas side significantly affected the steam side compared to vice versa. The partial heat load (80%) of recovery boiler and uneven inlet velocity caused a large recirculation zone in the superheater region. The uneven flue gas flow field was responsible for non-uniform heat flux distribution to superheater platens. For superheaters, the platens near side

walls received higher heat flux compared to the platens located in the middle region. The maximum difference of 83% was found for heat flux distribution to superheater platens. Furthermore, the local variations were noticed in superheater platens′ surface temperatures that were transferred from 1D-PM to CFD. The reasons could be local variations in generated superheated steam temperature values. In addition to this, a small portion of SH4 platens in the large recirculation zone was observed where superheated steam temperature was higher than the flue gas locally and reversed heat transfer occurred.

The integrated CFD/1D-PM simulations′ results including steam properties and superheater material temperature distribution were compared with standalone 1D-PM simulation. In the standalone 1D-PM simulation, the heat flux to superheaters was taken from integrated CFD/1D-PM simulations for the purpose of this comparison and uniformly distributed among the platens. The standalone 1D-PM simulation is a commonly used approach for superheated steam generation process.

The comparison study revealed that the non-uniform flue gas flow field substantially affected the platen-wise generated superheated steam temperature compared to steam mass flow rate distribution and pressure losses. The deviations in platen-wise steam superheating calculated by integrated CFD/1D-PM simulations were in the range of 45%- 122%. Whereas, the steam superheating values calculated by standalone 1D-PM simulation were almost uniform among the platens of an individual superheater, which were not accurate. However, the main steam pressure and temperature calculated by both integrated CFD/1D-PM simulations and standalone 1D-PM simulation deviated by 1.5% and 0.4% from the reference data respectively.

The calculated values for superheater material temperature during integrated CFD/1D-PM simulations and standalone 1D-PM simulation were compared with the measurements from the recovery boiler power plant. It was found that the standalone 1D-PM simulation predicted unrealistic results for superheater platens and their flow loops. On the other hand, the integrated CFD/1D-PM simulations showed that the non-uniform flue gas flow field in superheater region had large effect on platen-wise and flow loop-wise material temperature distribution. A considerable difference (1.0%-6.0%) was found between measured values and integrated CFD/1D-PM simulations′ results. The variation in flue gas flow field in superheater region during measurements and integrated CFD/1D-PM simulations was mainly responsible for these discrepancies.

Therefore, based on these observations, it is concluded that the integrated CFD/1D-PM simulations are feasible to solve the complex fluid-fluid heat transfer phenomena in superheater region with good accuracy. This integration modelling approach provides a new way to improve the performance and design of the superheaters. Hence, it enables us to increase the safety and thermal efficiency of recovery boilers. Whereas, either standalone CFD simulation or standalone 1D-PM simulation is not able to provide detailed knowledge about the effect of flue gas side on steam side and vice versa in superheater region of the recovery boiler.

5.2 Limitations and future recommendations

The limitations of this master thesis work are as follows:

1. The deposition on superheater platens and boiling surfaces is based on literature. In reality, it is very challenging to accurately measure the deposit thickness and its thermal conductivity because of complex recovery boiler operation as well as geometrical structure of superheater region.

2. The real recovery boiler operations are usually unsteady or time dependent. In this work, the steady-state RANS method was used for CFD simulation. Moreover, the grid convergence study was not performed to computationally verify the CFD simulation. The main reasons were large geometry of superheater region, intricacies associated with integrated CFD/1D-PM simulations and available computational time.

3. It was analysed that the inlet boundary condition profiles might have substantial effect on the flue gas flow field and the vortices in the superheater region under different boiler operating modes and in partial load conditions. This in turn can affect the heat flux distribution to superheaters. In this work, only one boiler operating mode was studied and sensitivity analysis was not performed. This point requires further analysis and the superheater region should be studied under various boiler operating conditions.

4. In the 1D-PM model, the inlet headers and outlet headers are modelled using T-junction component provided by Apros 6. The calculation procedure of T-junction was not verified. However, the T-junction component was utilized because it provided good simulation results compared to other modelling components including point and node.

The following future directions for this research work are identified:

1. A full scale time-dependent integrated CFD/1D-PM simulations including the black liquor combustion in lower furnace should be performed to further investigate the superheated steam generation process in a more precise way.

2. The integrated CFD/1D-PM modelling approach could be utilized to study the effects of rapid load change situations on flue gas flow field in superheater region, superheating process and superheater material temperature distribution. It could also be applied to understand the steam generation process in boiling surfaces of recovery boiler.

3. For headers, a CFD study should be performed to precisely understand the effects of their geometries on steam distribution. It will help to explore new possibilities for optimizing their performance and design.

4. The present integrated modelling approach is mainly developed for superheater region in recovery boilers. It could also be relevant to understand coupled fluid-fluid heat transfer phenomena in other large scale power generation units.

References

[1] Food and Agriculture Organisation of United Nations (FAO). *Forestry production and trade statistics.* Available at: http://www.fao.org/faostat/en/#data/FO. Accessed December 04, 2018.

[2] Tran, H., and Vakkilainen, E. *Advances in the Kraft chemical recovery process.* 3rd ICEP international colloquium on eucalyptus pulp, Belo Horizonte, Brazil. 2007. 4-7.

[3] Official Statistics of Finland (OSF): *Production of electricity and heat* [e-publication]. ISSN=1798-5099. Helsinki: Statistics Finland [referred: 11.12.2018]. Access method: http://www.stat.fi/til/salatuo/index_en.html

[4] Pöyry, *World Fibre Outlook up to 2030.* 2016. [Electronic publication].

[5] Alobaid, F., Mertens, N., Starkloff, R., Lanz, T., Heinze, C., and Epple, B. *Progress in dynamic simulation of thermal power plants.* Progress in Energy and Combustion Science (59). 2017. 79-162.

[6] Emara-Shabaik, H. E., Habib, M. A., and Al-Zaharna, I. *Prediction of risers' tubes temperature in water tube boilers.* Applied Mathematical Modelling (33.3). 2009. 1323-1336.

[7] Zima, W., Nowak-Ocłoń, M., and Ocłoń, P. *Simulation of fluid heating in combustion chamber waterwalls of boilers for supercritical steam parameters.* Energy (92). 2015. 117-127.

[8] Bhambare, K. S., Mitra, S. K., and Gaitonde, U. N. *Modeling of a coal-fired natural circulation boiler.* Journal of Energy Resources Technology (129.2). 2007. 159-167.

[9] Vakkilainen, E. *Continuous development of recovery boiler technology – 50 years of cooperation in Finland.* Suomen soodakattilayhdistys. 2014. 94-108.

[10] Patankar, S. V., and Spalding, D. B. *A calculation procedure for the transient and steady-state behavior of shell-and-tube heat exchangers.* Heat exchangers: design and theory source book (1). 1974.

[11] Yin, C., Rosendahl, L., and Condra, T. J. *Further study of the gas temperature deviation in large-scale tangentially coal-fired boilers.* Fuel (82.9). 2003. 1127-1137.

[12] Le Bris, T., Cadavid, F., Caillat, S., Pietrzyk, S., Blondin, J., and Baudoin, B. *Coal combustion modelling of large power plant, for NOx abatement.* Fuel (86.14). 2007. 2213-2220..

[13] Díez, L. I., Cortés, C., and Pallarés, J. *Numerical investigation of NOx emissions from a tangentially-fired utility boiler under conventional and overfire air operation.* Fuel (87.7). 2008. 1259-1269.

[14] Choi, C. R., and Kim, C. N. *Numerical investigation on the flow, combustion and NOx emission characteristics in a 500 MWe tangentially fired pulverized-coal boiler.* Fuel (88.9). 2009. 1720-1731.

[15] Drosatos, P., Nikolopoulos, N., Agraniotis, M., Itskos, G., Grammelis, P., and Kakaras, E. *Decoupled CFD simulation of furnace and heat exchangers in a lignite utility boiler.* Fuel (117). 2014. 633-648.

[16] Park, H. Y., Faulkner, M., Turrell, M. D., Stopford, P. J., and Kang, D. S. *Coupled fluid dynamics and whole plant simulation of coal combustion in a tangentially-fired boiler.* Fuel (89.8). 2010. 2001-2010

[17] Edge, P. J., Heggs, P. J., Pourkashanian, M., and Williams, A. *An integrated computational fluid dynamics–process model of natural circulation steam generation in a coal-fired power plant.* Computers & Chemical Engineering (35.12). 2011. 2618-2631.

[18] Schuhbauer, C., Angerer, M., Spliethoff, H., Kluger, F., and Tschaffon, H. *Coupled simulation of a tangentially hard coal fired* 700^oC *boiler.* Fuel (122). 2014. 149-163.

[19] Hovi, V., Huttunen, M., Karppinen, I., Pättikangas, T., Niemistö, H., Karvonen, L., Kallio, S., Tuuri, S., and Ylä-Outinen, V. *Integrated transient simulation of a BFB boiler with CFD models for the BFB furnace and dynamic system models for the steam cycle and boiler operation.* Energy Procedia (120). 2017. 508-515.

[20] Yang, Y., Bai, W., Wang, Y., Zhang, Y., Li, H., Yao, M., and Wang, H. *Coupled simulation of the combustion and fluid heating of a 300 MW supercritical CO2 boiler.* Applied Thermal Engineering (113). 2017. 259-267.

[21] Chen, T., Zhang, Y. J., Liao, M. R., and Wang, W. Z. *Coupled modeling of combustion and hydrodynamics for a coal-fired supercritical boiler.* Fuel (240). 2019. 49-56.

[22] Hovi, V., Pättikangas, T., and Riikonen, V. *Coupled one-dimensional and CFD models for the simulation of steam generators.* Nuclear Engineering and Design (310). 2016. 93-111.

[23] Saviharju, K., Pakarinen, L., Wag, K., and Välipakka, I. *Numerical modeling feedback in recovery boilers.* In Proceedings of the 2004 international chemical recovery conference (Vol. 1). 2004. 247-262.

[24] Leppänen, A., Välimäki, E., Oksanen, A., and Tran, H. *CFD-modeling of fume formation in kraft recovery boilers.* TAPPI Journal (12.3). 2013. 25-32.

[25] Leppänen, A., Tran, H., Taipale, R., Välimäki, E., and Oksanen, A. *Numerical modeling of fine particle and deposit formation in a recovery boiler.* Fuel (129). 2014. 45-53.

[26] Leppänen, A., Tran, H., Välimäki, E., and Oksanen, A. *Modelling fume deposit growth in recovery boilers: effect of flue gas and deposit temperature.* Journal of Science & Technology for Forest Products and Processes (4.1). 2014. 50-57

[27] Leppänen, A., and Välimäki, E. *Improving recovery boiler availability through understanding fume behavior.* TAPPI Journal (15.3). 2016. 187-193.

[28] Maakala, V., Järvinen, M., and Vuorinen, V. *Optimizing the heat transfer performance of the recovery boiler superheaters using simulated annealing, surrogate modeling, and computational fluid dynamics.* Energy (160). 2018. 361-377.

[29] Maakala, V., Järvinen, M., and Vuorinen, V. *Computational fluid dynamics modeling and experimental validation of heat transfer and fluid flow in the recovery boiler superheater region.* Applied Thermal Engineering (139). 2018. 222-238.

[30] Vakkilainen, E., Kuparinen, K., and Heinimö, J. *Large industrial users of energy biomass.* IEA Bioenergy Task (40). 2013. 2013 p.

[31] Adams, T. N. *Kraft recovery boilers.* TAPPI Press. 1997. 381 p. ISBN 0-9625985-9-3.

[32] Saviharju, K., Simonen, J., Simonen, L., Vakkilainen, E., and Mattelmäki, E. *Combustion air system for recovery boilers, burning spent liquors from pulping processes.* U.S. Patent No. 6,742,463 B2. 1 Jun. 2004.

[33] Bergman, T. L., Incropera, F. P., DeWitt, D. P., and Lavine, A. S. *Fundamentals of heat and mass transfer.* John Wiley & Sons, Inc. 2011. 1048 p. ISBN 13 978-0470-50197-9.

[34] The Babcock & Wilcox Company. *Steam: its generation and use.* Edition: 41. The Babcock & Wilcox Company. 2005. 1040 p. ISBN-10 0963457012. ISBN-13 978-0963457011.

[35] Collier, J. G., and Thome, J. R. *Convective boiling and condensation.* 3rd Edition. Clarendon Press. 1996. 640 p. ISBN-10 0198562969. ISBN-13 978-0198562962.

[36] Vakkilainen, E. *Kraft recovery boilers- Principles and practice.* Suomen Soodakattilayhdistys r.y. 2005. 244 p. ISBN 952-91-8603-7.

[37] Baehr, H. D., and Stephan, K. *Heat and mass transfer.* Springer-Verlag Berlin Heidelberg New York. 2006. 688 p. ISBN-10 3-540-29526-7. ISBN-13 978-3-540-29526-6.

[38] ANSYS SpaceClaim User's Guide.

[39] ANSYS Fluent User's Guide.

[40] ANSYS Fluent Meshing User's Guide.

[41] Launder, B. E., and Spalding, D. B. *Mathematical models of turbulence.* Academic press, London. 1972. ISBN 0-12-438050-6.

[42] VDI-Gesellschaft. *VDI Heat Atlas.* 2nd Edition. Springer-Verlag Berlin Heidelberg. 2010. 1551 p. ISBN 978-3-540-77876-9. e-ISBN 978-3-540-77877-6.

[43] Dorigon, L. J., Duciak, G., Brittes, R., Cassol, F., Galarça, M., and França, F. H. R. *WSGG correlations based on HITEMP2010 for computation of thermal radiation in non-isothermal, non-homogeneous H2O/CO2 mixtures.* International Journal of Heat and Mass Transfer (64). 2013. 863-873.

[44] Wessel, R. A., Denison, M. K., and Samretvanich, A. *The effect of fume on radiative heat transfer in kraft recovery boilers.* TAPPI Journal (83.7). 2000. 1-11.

[45] Li, B., Brink, A., and Hupa, M. *CFD investigation of slagging on a super-heater tube in a kraft recovery boiler.* Fuel Processing Technology (105). 2013. 149-153.

[46] Zbogar, A., Frandsen, F. J., Jensen, P. A., and Glarborg, P. *Heat transfer in ash deposits: A modelling tool-box.* Progress in Energy and Combustion Science (31.5-6). 2005. 371-421.

[47] Apros Process Simulation Software. Available at: http://www.apros.fi/en/.

[48] Faculty of Engineering and Applied Science, Mechanical and Materials Engineering, Queen's University, Canada. Available at: https://me.queensu.ca/People/Sellens/LossesinPipes.html.

[49] Rennels, D. C., and Hudson, H. M. *Pipe flow: A practical and comprehensive guide.* John Wiley & Sons. 2012. 289 p. ISBN 978-0-470-90102-1.

[50] Sharp, Z. B., Johnson, M. C., Barfuss, S. L., and Rahmeyer, W. J. *Energy losses in cross junctions.* Journal of Hydraulic Engineering (136.1). 2009. 50-55.

[51] Grace, T. M. *A critical review of computer modeling of kraft recovery boilers.* TAAPI Journal (79.7). 1995. 182-190.

[52] Engblom, M., Miikkulainen, P., Brink, A., and Hupa, M. *CFD-modeling for more precise operation of the kraft recovery boiler.* TAPPI journal (11.11). 2012. 19-27.

[53] EN 10216-2. *Seamless steel tubes for pressure purposes. Technical delivery conditions. Part 2: Non-alloy and alloy steel tubes with specified elevated temperature properties.* Edition-2013.